journal of the mechanical behavior of biomedical materials 151 (2024) 106370

Contents lists available at ScienceDirect

Journal of the Mechanical Behavior of Biomedical Materials

journal homepage: www.elsevier.com/locate/jmbbm

# Uncertainty quantification of the wall thickness and stiffness in an idealized dissected aorta

Lise Gheysen [a,*], Lauranne Maes [b], Annette Caenen [a,c], Patrick Segers [a], Mathias Peirlinck [d], Nele Famaey [b]

[a] Institute for Biomedical Engineering and Technology, Electronics and Information Systems, Ghent University, Belgium
[b] Biomechanics Section, Mechanical Engineering, KU Leuven, Belgium
[c] Cardiovascular Imaging and Dynamics, Department of Cardiovascular Sciences, KU Leuven, Belgium
[d] Department of BioMechanical Engineering, Faculty of Mechanical Engineering, Delft University of Technology, the Netherlands

ARTICLE INFO

*Keywords:*
Aortic dissection
Uncertainty quantification
Finite element analysis
Gaussian process regression
Vascular mechanics

ABSTRACT

Personalized treatment informed by computational models has the potential to markedly improve the outcome for patients with a type B aortic dissection. However, existing computational models of dissected walls significantly simplify the characteristic false lumen, tears and/or material behavior. Moreover, the patient-specific wall thickness and stiffness cannot be accurately captured non-invasively in clinical practice, which inevitably leads to assumptions in these wall models. It is important to evaluate the impact of the corresponding uncertainty on the predicted wall deformations and stress, which are both key outcome indicators for treatment optimization. Therefore, a physiology-inspired finite element framework was proposed to model the wall deformation and stress of a type B aortic dissection at diastolic and systolic pressure. Based on this framework, 300 finite element analyses, sampled with a Latin hypercube, were performed to assess the global uncertainty, introduced by 4 uncertain wall thickness and stiffness input parameters, on 4 displacement and stress output parameters. The specific impact of each input parameter was estimated using Gaussian process regression, as surrogate model of the finite element framework, and a δ moment-independent analysis. The global uncertainty analysis indicated minor differences between the uncertainty at diastolic and systolic pressure. For all output parameters, the 4$^{th}$ quartile contained the major fraction of the uncertainty. The parameter-specific uncertainty analysis elucidated that the material stiffness and relative thickness of the dissected membrane were the respective main determinants of the wall deformation and stress. The uncertainty analysis provides insight into the effect of uncertain wall thickness and stiffness parameters on the predicted deformation and stress. Moreover, it emphasizes the need for probabilistic rather than deterministic predictions for clinical decision making in aortic dissections.

## 1. Introduction

A type B aortic dissection is a disease that is characterized by a delamination of the inner part of the descending thoracic aortic wall, i.e. the intimal and a part of the medial layer. In the presence of one or more tears, this delamination allows the blood to flow along its normal pathway via the true lumen as well as along an alternative channel in between the dissected membrane and the remaining part of the wall, i.e. the false lumen. An example of such a patient-specific anatomy is shown in Fig. 1. Although the incidence rate is limited to 1.85/100,000, severe long-term complications such as aortic expansion, spinal cord ischemia, renal failure, paraplegia and aortic rupture can occur if the disease is not treated properly (DeMartino et al., 2018; Fattori et al., 2013; Mastroroberto et al., 2010). A common treatment for type B aortic dissections is thoracic endovascular aortic repair (TEVAR), implying that a stent-graft is implanted at the site of the proximal tear in order to seal off the false lumen. By sealing it off, surgeons aim to trigger complete thrombus formation of the false lumen, which results in healing of the dissection. Although TEVAR has a high acute success rate, the long-term success rate of complete false lumen thrombosis varies from 91% to values of only 22% (Gao et al., 2022; Nienaber et al., 2014; Xie et al., 2021). Moreover, while some of the remaining patients show a fully patent false lumen, partial thrombosis was observed for ca. 10% of the treated patients in most studies, which was found to result in a higher mortality

* Corresponding author.
*E-mail address:* Lise.Gheysen@UGent.be (L. Gheysen).

https://doi.org/10.1016/j.jmbbm.2024.106370
Received 27 March 2023; Received in revised form 21 December 2023; Accepted 1 January 2024
Available online 3 January 2024

rate (Nienaber et al., 2014; Trimarchi et al., 2013; Tsai et al., 2007; Xie et al., 2021). Furthermore, 20%–30% of the treated patients requires a re-intervention within the first year post-TEVAR and an expanded aortic diameter was observed for a similar fraction of the patients within the first year too (Fattori et al., 2013; Nienaber et al., 2011). It is, however, not yet elucidated how to determine *a priori* for which patients the desired outcome will be achieved.

Computational biomechanical models of the blood flow, dissected aortic wall and stent-graft deployment can contribute in gaining insight into the acute, mid- and long-term effect of TEVAR. Models of the dissected aortic wall with varying geometrical and material complexity have been proposed. Indeed, some geometrically patient-inspired and -specific dissected wall models have been developed as part of a fluid-structure-interaction model, which most often leads to a simplified single-layered soft tissue model with a linear elastic or an isotropic hyperelastic behavior (Alimohammadi et al., 2015; Bäumler et al., 2020; Chong et al., 2020; Keramati et al., 2020). Moreover, only the model of Bäumler et al. (2020) included the effect of pre-stress, confirming its large effect on the resulting model stresses and strains (Peirlinck et al., 2018a; Wang et al., 2017b). Others integrated advanced anisotropic hyperelastic material models, including the effect of elastin and collagen, with a medial and adventitial layer in their dissected wall model (Gultekin et al., 2019; Wang et al., 2017a, 2018). They mainly focused on the dissection progression, while limiting the geometrical complexity. In this respect, Zhang et al. (2022) recently modelled dissected membrane buckling, caused by an artificially induced dissection, in a residually stressed, though unloaded, circular sample of the aortic wall. In an attempt to include dissection progression in the model, Rolf-Pissarczyk et al. (2021) developed a constitutive law that includes the degradation of the elastic fibers that interconnect the elastic lamellae in the media and applied it to an axially stretched and pressurized idealized dissected wall. No models were found that accounted for both the geometrical complexity and the constituent-specific and, consequently, anisotropic material behavior, which might affect the result when aiming at the long-term outcome prediction of type B dissections.

Moreover, in most of these models, assumptions regarding the material behavior, the thickness of the non-dissected aortic wall and the fraction of the dissected membrane and, if applicable, the medial thickness have inevitably been made. Often, the acquired values were adopted from literature, as an idealized geometry was considered or no patient-specific structural data was available. In the current clinical practice, these thickness and stiffness parameters can, indeed, not be retrieved from the standard imaging modalities, which are mainly contrast-enhanced CT scans with typical image resolutions in the axial plane in the order of 0.6 mm–1.0 mm for qualitative scans, according to the authors' experience. Insight into the effect of these parameters on the predicted output is essential when envisioning models that assist in the clinical decision making for the treatment of type B aortic dissections. To the best of the authors' knowledge, the uncertainty induced by an unknown true wall thickness and stiffness of the dissected aorta on finite element model output parameters has not yet been investigated.

Therefore, this study aims (i) to develop an idealized dissected aortic wall framework that includes an anisotropic hyperelastic material model with a medial and adventitial layer that (ii) enables the global and parameter-specific uncertainty quantification of the characteristic deformation patterns and maximum principal stress values with respect to varying wall stiffness and thickness parameters.

## 2. Methods

An overview of the main uncertainty analysis is presented in Fig. 2. First, section 2.1. describes the general model framework of the

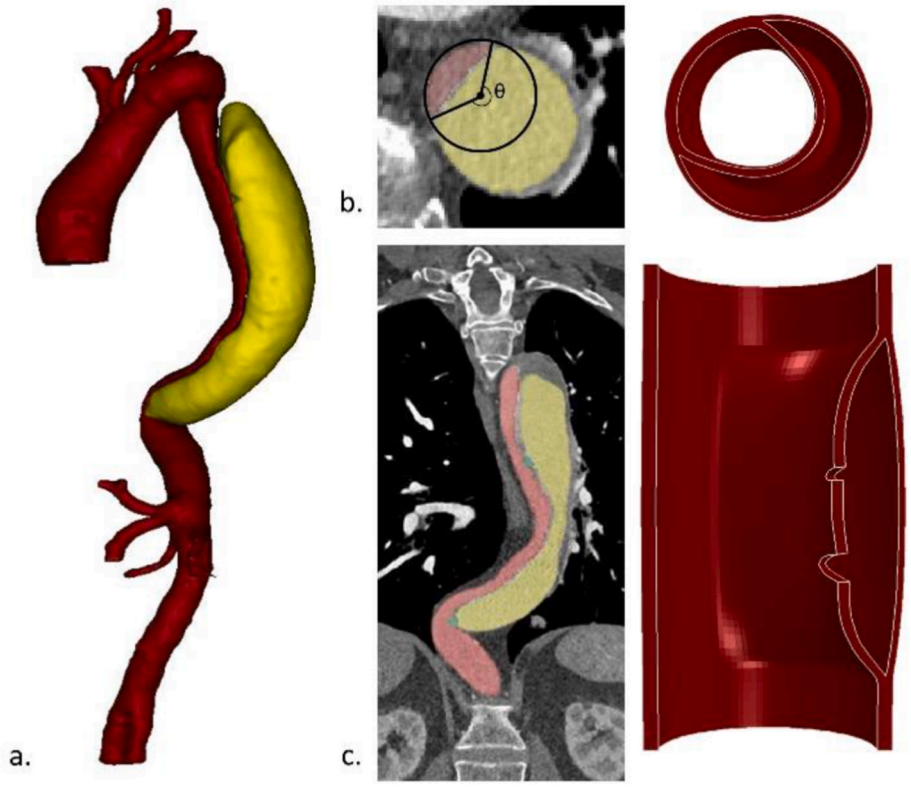


**Fig. 1.** Overview of a patient-specific anatomy of a type B aortic dissection and the corresponding views of the idealized dissection model. (a) 3-dimensional segmentation of an aortic dissection obtained from a patient-specific CT scan, together with (b) an axial and (c) a coronal slice and the corresponding view of the dissected wall model. On the CT slices, the true lumen is indicated in red, the false lumen in yellow and the tears in green. On (b) the axial slice, the best-fit circle of the intact true lumen wall is indicated together with the circumferential angle θ that covers the dissected membrane.

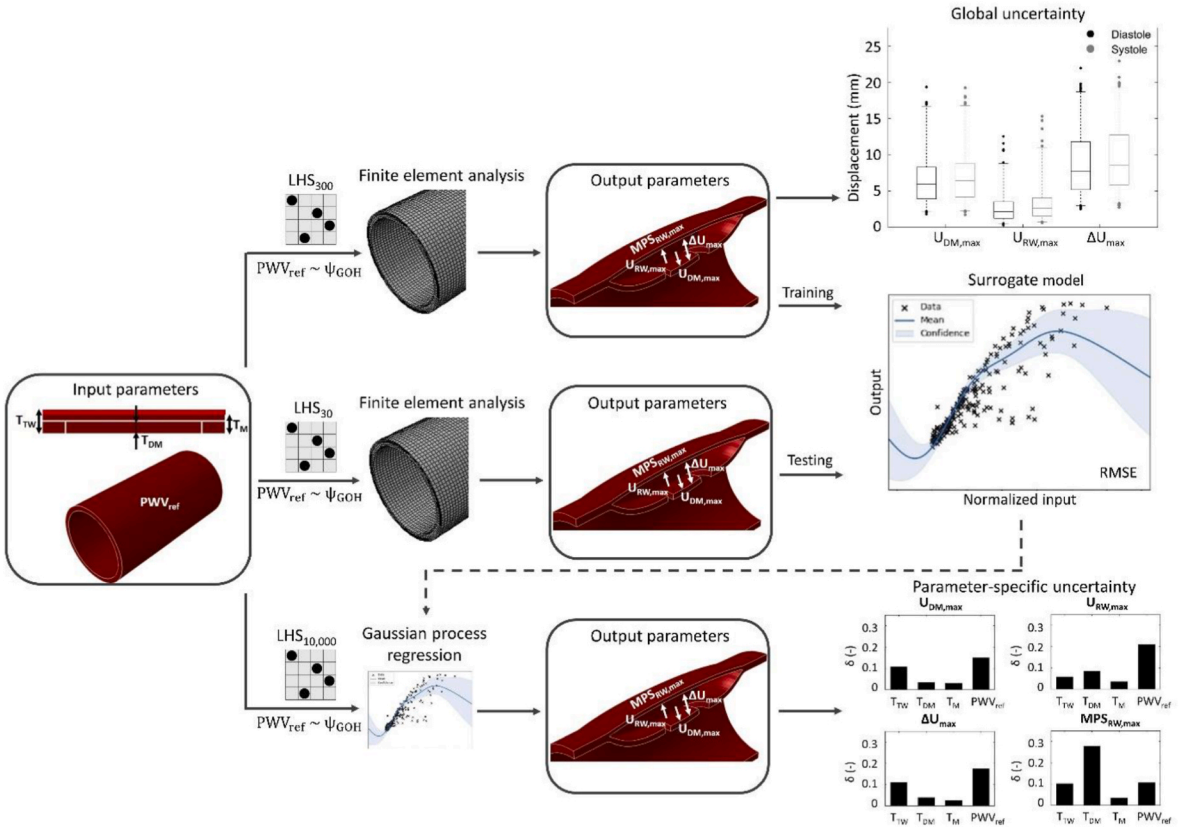


**Fig. 2.** Overview of the general workflow for the global and parameter-specific uncertainty quantification. The input parameters $T_{TW}$, $T_{DM}$, $T_M$ and $PWV_{ref}$ refer, respectively, to the total wall thickness, the relative dissected membrane thickness, the relative medial thickness and the pulse wave velocity of the reference model. The 4 output parameters $U_{DM,max}$, $U_{RW,max}$, $\Delta U_{max}$ and $MPS_{RW,max}$ indicate the maximal displacement of the dissected membrane, the maximal displacement of the remaining wall, the maximal distance between the dissected membrane and remaining wall and the maximal principal Cauchy stress at the maximal displacement of the remaining wall. The Latin hypercube samplings with 30, 300 and 10,000 samples are abbreviated as $LHS_{30}$, $LHS_{300}$ and $LHS_{10,000}$.

dissected aortic wall. This model framework is, in section 2.2., applied to assess the uncertainty induced by unknown thickness and stiffness parameters (section 2.2.1.) on the wall displacement and stress (section 2.2.2.). In section 2.2.3., the uncertainty is assessed on a global level, i.e. related to the combined effect of the considered input parameters for a set of 300 finite element analyses. In section 2.2.4., the uncertainty analysis is extended to the parameter-specific level, which requires the development of a surrogate model to generate the necessary large number (10,000) of model results. Finally, section 2.3. considers the impact of some intrinsic assumptions of the model framework.

### 2.1. Dissected wall model framework

#### 2.1.1. Geometry and mesh

The dissected wall model was generated starting from a cylindrical geometry with a length of 60 mm and a diameter of 27.3 mm, which is in the range of reported diameters of descending thoracic aortas without dissection (McComb et al., 2016; Rylski et al., 2018; Yamauchi et al., 2018). The false lumen, with an axial length of 40 mm, and the tears were inserted at predetermined locations, thus creating a dissected membrane and a remaining wall (Fig. 3). The circumferential false lumen size was determined based on the pre-operative CT scans of a

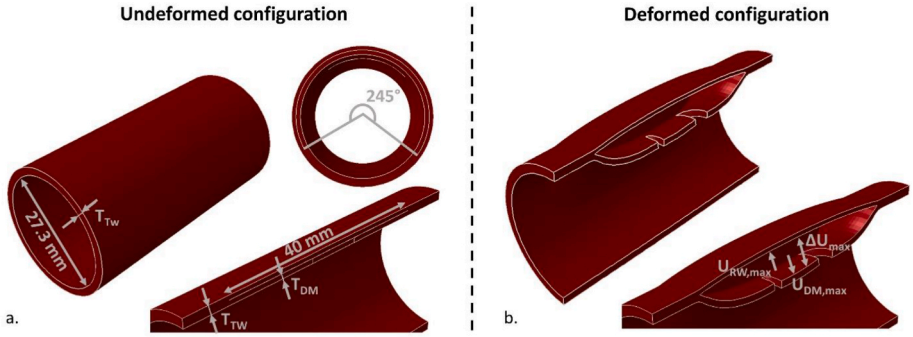


**Fig. 3.** Geometry of the idealized dissection model in the (a) undeformed and (b) deformed configuration at diastolic pressure (80 mmHg). On the undeformed configuration, $T_{TW}$ and $T_{DM}$, i.e. the total wall and the relative dissected membrane thickness, are indicated. On the deformed configuration, the displacement output parameters are visualized, with $U_{DM,max}$, $U_{RW,max}$ and $\Delta U_{max}$ being, respectively, the maximal displacement of the dissected membrane, the maximal displacement of the remaining wall and the maximal distance between the dissected membrane and the remaining wall.

**Table 1**
Overview of the applied input ranges for the Latin hypercube sampling and the full factorial design, performed to couple the GOH parameters for the media and adventitia to the $PWV_{ref}$, similar to Gheysen et al. (2023). The corresponding references are mentioned as well.

| Parameter | Meaning | Range | | | Reference |
|---|---|---|---|---|---|
| | | LB | UB | Mean | |
| **Thickness** | | | | | |
| $T_{TW}$ (mm) | Total wall thickness | 1.30 | 2.50 | 1.90 | (Eikendal et al., 2018; Gao et al., 2017; Li et al., 2004; Mani et al., 2009; Manopoulos et al., 2018; Mensel et al., 2014; Schriefl et al., 2012; Weisbecker et al., 2012) |
| $T_M$ (% $T_{TW}$) | Medial thickness, relative to total wall thickness | 65 | 85 | 75 | (Humphrey, 2013; Manopoulos et al., 2018; Schriefl et al., 2012; Weisbecker et al., 2012), |
| $T_{DM}$ (% $T_M$) | Dissected membrane thickness, relative to media thickness | 50 | 90 | 70 | (Humphrey, 2013; Manopoulos et al., 2018) |
| **Stiffness** | | | | | |
| $PWV_{ref}$ (m/s) | Pulse wave velocity of reference cylinder | 4.0 | 12.0 | | (The Reference Values for Arterial Stiffness' collaboration, 2010) |
| $c_{10M}$ (MPa) | Elastin stiffness in media | 0.005 | 0.025 | | (Jadidi et al., 2020; Weisbecker et al., 2012) |
| $k_{1M}$ (MPa) | Collagen stiffness in media | 0.0002 | 1.0 | | (Jadidi et al., 2020; Weisbecker et al., 2012) |
| $k_{2M}$ (−) | Collagen stiffening in media | 4.0 | 35.0 | | (Jadidi et al., 2020; Weisbecker et al., 2012) |
| $\alpha_M$ (°) | Mean fiber angle in media | 0 | 45 | | (Niestrawska et al., 2016; Schriefl et al., 2012) |
| $\kappa_M$ (−) | Fiber dispersion in media | 0 | 1/3 | | (Gasser et al., 2006) |
| $\alpha_A$ (°) | Mean fiber angle in adventitia | 45 | 90 | | (Niestrawska et al., 2016; Schriefl et al., 2012) |
| $\kappa_A$ (−) | Fiber dispersion in adventitia | 0 | 1/3 | | (Gasser et al., 2006) |

LB = lower bound; UB = upper bound.

patient-specific case with a type B dissection, obtained from the University Hospital of Düsseldorf with consent of the local ethical committee (reference number: 2017064325) (Logghe et al., 2021). To do so, the healthy pre-dissection diameter was estimated as the diameter of the best-fit circle based on the curvature of the true lumen wall, for each axial CT slice of the dissection in which the true and false lumen could be distinguished (Fig. 1(b)). The circumferential false lumen size was then determined as the angle, within that best-fit circle, that covered the section with dissected wall tissue. Calculating the median angle over the axial CT slices, lead to a circumferential false lumen size of 245°.

### 2.1.2. Material behavior

The dissected aortic wall contained a medial and adventitial layer, both behaving as an incompressible anisotropic hyperelastic Gasser-Ogden-Holzapfel (GOH) material (Gasser et al., 2006). The strain energy density function of each layer, $\psi_{layer}$, was defined as

$$\psi_{layer} = c_{10}\left(I_1^e - 3\right) + \frac{k_1}{2k_2}\left(\sum_{i=4,6} e^{k_2\left(\kappa I_1^c + (1-3\kappa) I_i^c - 1\right)^2} - 1\right) \quad \text{(EQ.1)}$$

with $c_{10}$ representing the elastin shear modulus, $k_1$ the collagen fiber stiffness, $k_2$ the intrinsic collagen fiber stiffening, $\kappa$ the collagen fiber dispersion and $\alpha$ the mean collagen fiber angle with respect to the circumferential direction. The 1st, 4th and 6th invariant of the Cauchy-Green tensor **C** are, respectively, indicated by $I_1$, $I_4$ and $I_6$. The superscripts e and c, respectively, refer to elastin and collagen.

Physiological ranges for the medial and adventitial material parameters were determined, based on reported uniaxial and biaxial experimental data of (descending) thoracic aortas without dissection (Table 1) (Jadidi et al., 2020; Weisbecker et al., 2012). The stiffness of the elastin and collagen of the adventitial layer, indicated with index A, was assumed to depend on that of the medial layer, indicated with index M, by accounting for the relative area fraction of elastin and collagen in both material layers (Iliopoulos et al., 2009). Moreover, all collagen fibers of the aortic wall were assumed to have the same intrinsic stiffening and, hence, $k_2$. Combining these assumptions with EQ.1 resulted in

$$\psi_M = c_{10M}\left(I_1^e - 3\right) + \frac{k_{1M}}{2k_2}\left(\sum_{i=4,6} e^{k_2\left(\kappa_M I_1^c + (1-3\kappa_M) I_i^c - 1\right)^2} - 1\right)$$
$$\psi_A = c_{10A}\left(I_1^e - 3\right) + \frac{k_{1A}}{2k_2}\left(\sum_{i=4,6} e^{k_2\left(\kappa_A I_1^c + (1-3\kappa_A) I_i^c - 1\right)^2} - 1\right) \quad \text{(EQ.2)}$$

with $c_{10A} = 0.34 c_{10M}$ and $k_{1A} = 1.17 k_{1M}$.

The *in vivo* pre-stretched state of the aortic wall was integrated using a Matlab (The MathWorks Inc., USA) implementation of the deposition stretch algorithm of Famaey et al. (2018) for thick-walled cylinders (Ogden, 2017). The collagen and axial elastin deposition stretch was assumed to remain constant throughout the geometry and equal to 10%, representative for the descending aorta of a 65 year old person, which corresponds to the average age of a patient with a type B aortic dissection (Horny et al., 2014; Logghe et al., 2021).

The selection of GOH parameters was coupled to the pulse wave velocity of a reference cylinder ($PWV_{ref}$) at diastolic pressure (80 mmHg). By using $PWV_{ref}$ as a representation of the aortic wall stiffness, GOH parameter combinations that lead to a physiological material behavior were ensured. Therefore, a full factorial design was performed on discretized physiological ranges of the GOH parameters, to eliminate incompatible combinations (Table 1) (Gheysen et al., 2023). For each combination of the full factorial design, the deposition stretches at 80 mmHg were calculated for a cylindrical thick-walled reference model with dimensions corresponding to the average values of the applied thickness ranges as reported in Table 1 (Ogden, 2017). The combinations leading to a tensile circumferential elastin deposition stretch ($g_{e,circ}$) throughout the wall were retained as they complied with the assumption that elastin has been stretched during human development (Powell et al., 1992; Shapiro et al., 1991). The pulse wave velocity at 80 mmHg was then calculated for the resulting GOH parameter combinations. Consequently, the GOH parameter combination with the $PWV_{ref}$ that best matched the required pulse wave velocity, was selected.

#### 2.1.3. Finite element analysis

The *in vivo* mechanical loading state of the dissected aorta at a physiological diastolic (80 mmHg) and systolic (120 mmHg) blood pressure was modelled using a finite element analysis in Abaqus/Implicit (Dassault Systèmes, France). The cylindrical geometry (section 2.1.1.) was meshed with hybrid hexahedral elements, using the in-house developed software pyFormex for geometrical operations and pre- and post-processing of finite element analyses (Bols et al., 2016; Peirlinck et al., 2018b). Herein, the tears and false lumen were implemented as unconnected elements at the corresponding interfaces (Fig. 3).

To compute the deformed dissected wall configuration, first, the deposition stretches were calculated for the healthy cylindrical aortic wall, i.e. without tears or false lumen, at the location of the element centroid (section 2.1.1.). The *in vivo* diastolic configuration was then obtained by applying the resulting deposition stretches to the dissected wall model together with the diastolic pressure, both in the true and false lumen. Since the mesh consists of unconnected elements at the tears and the false lumen, this allowed the dissected membrane to deform as a result of the release of the residual stresses. This approach ensured a realistic deformation of the dissected wall. Next, the intra-arterial pressure in the true and false lumen was further increased to systolic pressure. As the same pressure was applied to the true and false lumen, no net pressure gradient over the dissected membrane was assumed. At the proximal and distal end of the model, only radial displacement was allowed.

To ensure mesh-independent results, a mesh sensitivity study, with the number of elements ranging from 36,000 to 162,000, was performed for a reference geometry with average wall thickness parameters (Table 1) and a stiffness corresponding to a physiological pulse wave velocity of 5 m/s (The Reference Values for Arterial Stiffness' collaboration, 2010).

### 2.2. Uncertainty quantification of unknown thickness- and stiffness parameters

#### 2.2.1. Input parameters and sampling

The uncertainty related to the unknown material stiffness and wall thickness was quantified using 4 input parameters: (i) the total wall thickness ($T_{TW}$; mm); (ii) the medial thickness relative to $T_{TW}$ ($T_M$; % of $T_{TW}$); (iii) the dissected membrane thickness relative to the $T_M$ ($T_{DM}$; % of $T_M$) and (iv) $PWV_{ref}$ as representation of the aortic wall stiffness. $T_M$ and $T_{DM}$ were expressed relative to $T_{TW}$ and $T_M$, respectively, to ensure parameter independence. The use of $PWV_{ref}$ allows a continuous sampling of the stiffness parameter, while avoiding incompatible GOH parameter combinations (section 2.1.2.).

The 4-dimensional input parameter space was sampled using a Latin hypercube sampling, which is more efficient and robust compared to a random Monte Carlo sampling (Helton and Davis, 2003). This sampling implies that each input parameter was divided into intervals of equal probability, which are represented by one sample only. A uniform probability distribution was assumed for the 4 independent input parameters.

Note that each sample contains a $PWV_{ref}$, obtained for a reference cylinder with an average $T_{TW}$ and $T_M$, and thickness values that, most likely, deviate from these average thicknesses. As the deposition stretch has to reflect the effective residual stresses in the considered sample geometry, the corresponding $g_{e,circ}$ was calculated for the selected GOH parameters, based on $PWV_{ref}$, and the sample thicknesses, instead of the reference model with average thickness parameters. Consequently, the sample $g_{e,circ}$ might be compressive, while only tensile $g_{e,circ}$ are considered to be physiological (section 2.1.2.). Therefore, samples leading to a compressive $g_{e,circ}$ were excluded from the uncertainty analysis.

#### 2.2.2. Output parameters

In total, 4 output parameters were considered. To determine the uncertainty related to the dissected wall deformation, the following output parameters were determined: (i) the maximal displacement of the dissected membrane relative to the healthy cylindrical configuration, $U_{DM,max}$, (ii) the maximal displacement of the remaining wall relative to the healthy configuration, $U_{RW,max}$, and (iii) the maximal distance between initially coinciding nodes of the dissected membrane and remaining wall, $\Delta U_{max}$, which corresponds to the maximal distance between the dissected membrane and remaining wall as visible on clinical CT scans. Furthermore, (iv) the maximum principal Cauchy stress at the location of $U_{RW,max}$, $MPS_{RW,max}$, was assessed, by averaging the maximal principal stress over the integration points of the elements that surround the considered node and the corresponding nodes on the same radial axis throughout the remaining wall. It is noteworthy, that $MPS_{RW,max}$ does not necessarily correspond to the maximal stress in the remaining wall. However, as the acute dissected wall was of interest, rather than the potential of the dissection to progress, the choice was made to exclude the regions at the false lumen boundaries and to focus on the stress at the location of the largest remaining wall deformation, which is often essential in the estimation of the rupture risk.

#### 2.2.3. Global uncertainty quantification based on finite element analyses

The combined effect of the uncertainty on the 4 independent input parameters was assessed using a Latin hypercube with 300 samples ($LHS_{300}$). For each sample with a corresponding $g_{e,circ} \geq 1.0$ (section 2.2.1.), a finite element analysis was performed with the dissected wall model framework that was adapted according to the considered stiffness and thickness parameters. For each of the 4 output variables, the median value as well as the interquartile range (IQ) and the interval between the minimum and maximum value (min-max) over the $LHS_{300}$ were determined.

#### 2.2.4. Parameter-specific uncertainty quantification based on surrogate models

To quantify the parameter-specific uncertainty related to the idealized dissected wall model, large amounts of samples need to be assessed, which would be too computationally expensive when using finite element analyses. Therefore, the development of a surrogate model (section 2.2.4.1.) is discussed before continuing with the parameter-specific uncertainty analysis (section 2.2.4.2.).

*2.2.4.1. Surrogate model of the dissected wall.* A surrogate model was developed based on the input from the $LHS_{300}$ and the corresponding results obtained with the finite element analyses. As the relatively limited amount of input samples might introduce uncertainty in the surrogate model, it was opted to train a Gaussian process regression model, which accounts for the uncertainty in the surrogate model itself, instead of a regular neural network, using the open-source package GPy in Python 3.7 (Gpy, 2012).

Here, an important consideration is that it is the aim of the Gaussian process regression to surrogate the finite element analysis as accurately as possible. Given that perspective, $PWV_{ref}$ (as an encompassing material parameter) was replaced by the corresponding 7 GOH parameters and the calculated $g_{e,circ}$ at the inner radius of the sample geometry, similar to the input for the finite element analyses. Thus, when combined with the 3 thickness input parameters, this results in a Gaussian process with 11 input parameters. The input parameters were normalized between 0 and 1, by

$$x_{i,norm} = \frac{x_i - x_{i,min}}{x_{i,max} - x_{i,min}} \quad \text{(EQ.3)}$$

with $x_{i,norm}$, $x_{i,min}$ and $x_{i,max}$ being the respective normalized, minimal and maximal value of input parameter $X_i$. For the output parameters, the mean was subtracted in order to comply to the zero-mean assumption during the training of the Gaussian process. No further normalization was applied, to facilitate the interpretation of the predicted output.

The Gaussian process was trained by using a radial basis function of the form

$$k(\mathbf{x_m}, \mathbf{x_n}) = \sigma^2 e^{-\frac{1}{2}\frac{\|\mathbf{x_m}-\mathbf{x_n}\|^2}{L^2}} \quad \text{(EQ.4)}$$

as kernel, with $\mathbf{x_m}$ and $\mathbf{x_n}$ two points in the multi-dimensional input space, σ the variance and L the length scale, both being hyperparameters of the Gaussian process. While the kernel contains one σ parameter, an anisotropic kernel with a different length scale for each input parameter was included. The hyperparameters were determined by optimizing the log-likelihood during the training process in maximally 100,000 iterations. The process was trained on the available samples of the $LHS_{300}$ and a new, randomly generated, $LHS_{30}$ was used as test set. The root mean squared error (RMSE) was calculated for the test set. A RMSE≤1.0 mm was pursued for the displacement output parameters to limit the mean error to a representative pixel size of a clinical CT scan. No predefined RMSE for $MPS_{RW,max}$ was assigned, as not much is currently known regarding the stress in a dissected wall.

*2.2.4.2. Delta moment-independent analysis.* The trained surrogate model was used to perform a global sensitivity analysis in order to gain insight into the effect of the uncertainty on the individual input parameters. Therefore, the trained Gaussian processes were applied to calculate the output of a Latin hypercube sampling of 10,000 samples ($LHS_{10,000}$) based on the 4 independent input parameters ($T_{TW}$, $T_M$, $T_{DM}$ and $PWV_{ref}$) as discussed in section 2.2.1. To be consistent with the finite element analyses, the GOH parameter combination that lead to the closest pulse wave velocity compared to the required $PWV_{ref}$ was determined for each of the 10,000 samples, the corresponding sample $g_{e,circ}$ was calculated and samples leading to $g_{e,circ}$<1.0 were excluded (section 2.2.1.). Of the remaining samples, those leading to an output value in the lower and upper 2.5% were excluded to limit the weight attributed to these extreme values, which might potentially be the result of regions of large uncertainty in the Gaussian process and, thus, less reliable.

The remaining samples of the $LHS_{10,000}$, combined with the determined results for the 4 considered output parameters, were subjected to a δ moment-independent analysis, using the SALib python package (Borgonovo, 2007; Herman and Usher, 2017). This analysis considers the importance of each input parameter, by taking into account the complete output distribution, instead of a moment of the distribution, i.e. a characteristic of the distribution shape as the variance or skewness. Indeed, $\delta_i$ considers the expected shift between the unconditional and conditional output distribution for an input parameter $X_i$ and is, thus, defined as

$$\delta_i = \frac{1}{2} E_{X_i}[s(X_i)] \text{ with}$$

$$s(X_i) = \int \left| f_Y(y) - f_{Y|X_i}(y) \right| dy \text{ and}$$

$$E_{X_i}[s(X_i)] = \int f_{X_i}(x_i)[s(X_i)]dx_i. \quad \text{(EQ.5)}$$

$E_{Xi}$ indicates the expected value of shift s for input parameter $X_i$, which considers the difference between $f_Y(y)$ and $f_{Y|Xi}(y)$ that, respectively, indicate the unconditional distribution of output Y and the conditional distribution Y for a known input parameter $X_i$.

### 2.3. Additional sources of uncertainty

In this section, the impact of some intrinsic assumptions of the model framework and their contribution to the output uncertainty is considered.

#### 2.3.1. Pressure gradient

The standard model framework does not include a pressure gradient over the dissected membrane, while pressure differences of 3 mmHg between the true and false lumen have been measured *in vivo* (Pirola et al., 2019). To assess the impact of neglecting the pressure gradient, a pressure difference of 3 mmHg over the dissected membrane was applied to 10 randomly selected samples of the $LHS_{300}$ (supplementary material). Similar to the *in vivo* measurements, the higher pressure was located in the false lumen in diastole and in the true lumen during systole (Pirola et al., 2019). The difference in output was assessed using the median value of the difference between the results obtained with and without pressure gradient at the considered loading state, i.e. either diastole or systole. The width of the min-max range was determined too to assess the effect on the output uncertainty. Moreover, by taking the difference between $U_{DM,max}$ at diastolic and systolic pressure with the inclusion of the pressure gradient, the dissected membrane movement was estimated.

#### 2.3.2. Axial dissection length

Compared to *in vivo* observations, where type B dissections often distend from the arch to the abdominal aorta, an axial dissection length of 40 mm is rather limited (Bäumler et al., 2020; Ganten et al., 2009; Nienaber et al., 2014). To assess the effect of this assumption on the output parameters, a slice model of the idealized dissected wall, i.e. without tears or proximal and distal connection between the dissected membrane and the remaining wall, with an axial length of 5 mm was developed. Accordingly, this slice model represents an infinitely long dissection and, thus, the expected upper boundary of the potential dissected membrane displacement for the considered samples. The slice model was applied to 10 samples, randomly chosen from $LHS_{300}$, i.e. the same samples as in section 2.3.1. (supplementary material). The impact on the output parameters was determined as the median difference between the result of the idealized dissected wall and slice model. The effect on the output uncertainty range was considered by using the min-max range.

## 3. Results

### 3.1. Reference dissected wall model

The results of the idealized dissected wall model are similar for the reference geometry irrespective of the element number. Indeed, the results of the finer meshes (with 54,000 to 162,000 elements) deviate 0.5%–2.8% from those of the coarsest mesh (with 36,000 elements) for the considered wall displacement and stress output parameters. The computational time increases from 13 min with 5 cores to 55 min with 16 cores (250 GiB RAM and 180 GB local storage per core) with an increasing element number. Due to the minor differences in the output parameters, it is opted to perform the uncertainty analysis with the coarsest mesh to minimize the computational cost.

Fig. 4 illustrates the deformation and maximal principal wall stress obtained for the reference model with the final (coarsest) mesh at diastolic and systolic pressure. The maximal deformation of the remaining wall and the dissected membrane is observed at the central part of the dissection. While a local increase in maximal principal wall stress is observed in the remaining wall at the location of separation with the dissected membrane, the central part of the membrane shows negligible stresses.

### 3.2. Global uncertainty quantification based on finite element analyses

Out of the 300 samples from the $LHS_{300}$, 237 useful results are obtained. From the 63 excluded samples, 25 do not fulfill the convergence criteria of the finite element analysis, while 38 samples result in non-physiological deposition stretches ($g_{e,circ}$<1.0) when applying the algorithm to the sample instead of the reference geometry. The non-physiological deposition stretches are obtained for sample geometries with a larger absolute medial thickness than the reference model. Fig. 5

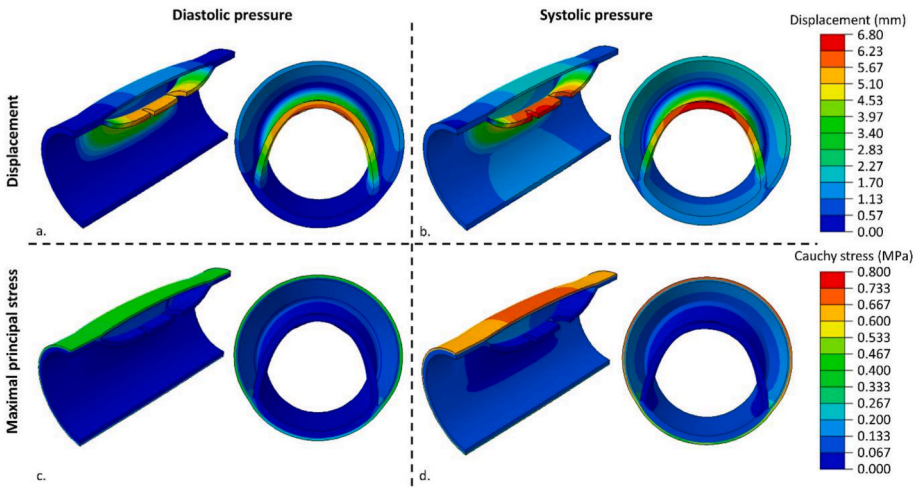


**Fig. 4.** Overview of the resulting (a, b) displacement magnitude, with respect to the undeformed configuration, and (c, d) maximal principal wall stress of the reference model at (a, c) diastolic (80 mmHg) and (b, d) systolic (120 mmHg) pressure.

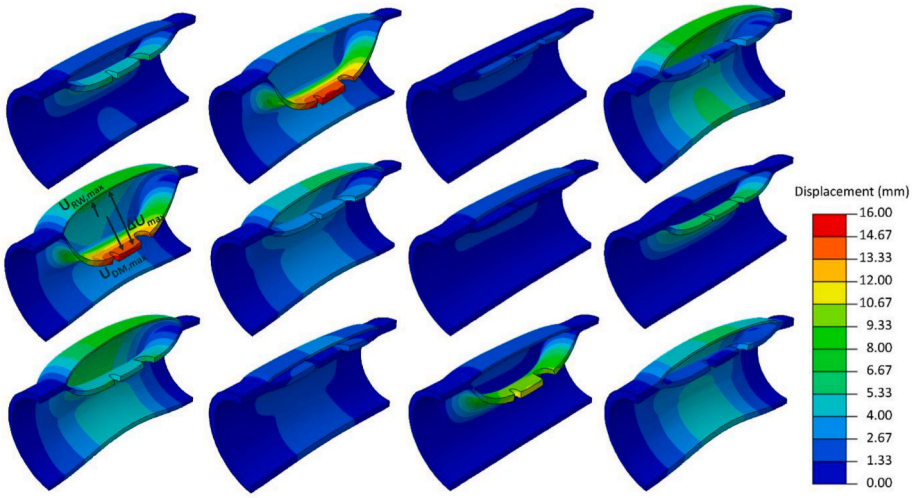


**Fig. 5.** Overview of the deformed dissected wall configuration at diastolic pressure (80 mmHg) of 12 example samples of the $LHS_{300}$. The color scale indicates the displacement of the nodes with respect to the initial cylindrical configuration. The output parameters $U_{DM,max}$, $U_{RW,max}$ and $\Delta U_{max}$ are indicated for one example configuration and, respectively, correspond to the maximal displacement of the dissected membrane, the maximal displacement of the remaining wall and the maximal distance between the dissected membrane and remaining wall.

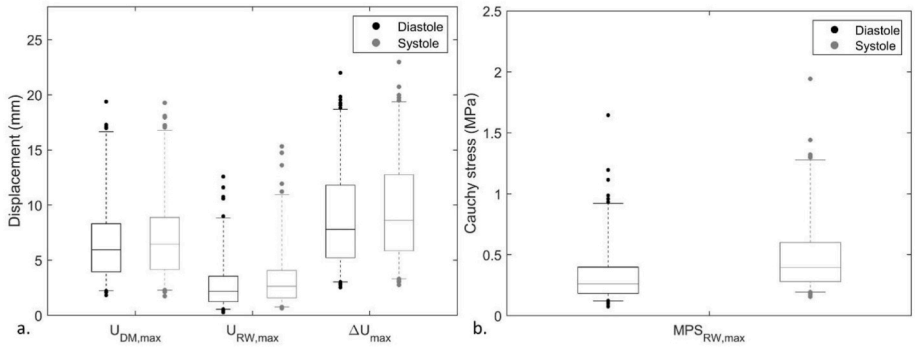


**Fig. 6.** Boxplots of the 237 deformed configurations at diastolic (80 mmHg) and systolic (120 mmHg) pressure. The output (a) displacements $U_{DM,max}$, $U_{RW,max}$ and $\Delta U_{max}$ and (b) Cauchy stress $MPS_{RW,max}$ represent the maximal displacement of the dissected membrane, the maximal displacement of the remaining wall, the maximal distance between the dissected membrane and remaining wall and the maximal principal Cauchy stress at the maximal displacement of the remaining wall. The span of the whiskers represents the central 95% of the output values.

**Table 2**
Median value, interquartile (IQ) and min-max ranges of $U_{DM,max}$, $U_{RW,max}$ and $\Delta U_{max}$ and $MPS_{RW,max}$ of the 237 deformed configurations at diastolic (80 mmHg) and systolic (120 mmHg) pressure. The IQ and min-max ranges are expressed as the absolute deviation with respect to the corresponding median value.

| | Diastole | | | Systole | | |
|---|---|---|---|---|---|---|
| Output | Median | IQ range | min-max range | Median | IQ range | min-max range |
| $U_{DM,max}$ (mm) | 5.95 | [-1.99; 2.28] | [-4.13; 13.44] | 6.46 | [-2.29; 2.36] | [-4.72; 12.81] |
| $U_{RW,max}$ (mm) | 2.19 | [-0.96; 1.31] | [-1.91; 10.38] | 2.64 | [-1.06; 1.40] | [-2.01; 12.68] |
| $\Delta U_{max}$ (mm) | 7.78 | [-2.55; 4.01] | [-5.24; 14.22] | 8.62 | [-2.76; 4.12] | [-5.87; 14.36] |
| $MPS_{RW,max}$ (MPa) | 0.26 | [-0.08; 0.14] | [-0.18; 1.39] | 0.40 | [-0.12; 0.20] | [-0.24; 1.55] |

illustrates the displacement magnitude of 12 example deformed configurations at diastolic pressure, with respect to the initial cylindrical configuration. Some examples of representative maximal principal stress patterns are shown in appendix A. While the complete overview of input and output parameters is reported in supplementary material, the median values and the IQ and min-max uncertainty ranges of the 237 samples for the 4 output parameters, at the considered pressures, are shown in Fig. 6 and summarized in Table 2. Larger median displacements were obtained for parameters involving the dissected membrane ($U_{DM,max}$ and $\Delta U_{max}$) compared to those obtained for $U_{RW,max}$ at both pressure levels. When going from diastolic to systolic pressure, the median displacements show a maximal increase of 0.84 mm. Similarly, the highest median $MPS_{RW,max}$ was found at 120 mmHg. The fraction of the IQ range, relative to the min-max range, varies from 24% to 34% for the displacement parameters that include the dissected membrane deformation ($U_{DM,max}$ and $\Delta U_{max}$) and from 14% to 18% for parameters related to the remaining wall ($U_{RW,max}$ and $MPS_{RW,max}$), at both diastole and systole. Higher fractions were observed for the 4$^{th}$ quartile for all output parameters, with intervals ranging from 51% (for $\Delta U_{max}$ at systolic pressure) to 80% (for $MPS_{RW,max}$ at diastolic pressure).

### 3.3. Parameter-specific uncertainty quantification based on surrogate models

#### 3.3.1. Surrogate model of the dissected wall

The Gaussian processes are trained on the 237 samples of the $LHS_{300}$ and tested on 26 samples, obtained from the $LHS_{30}$ after excluding the samples with a $g_{e,circ}<1.0$ for the sample geometry. The RMSE of the Gaussian processes varies from 0.73 mm to 1.43 mm for the displacement output parameters and from 0.075 MPa to 0.120 MPa for $MPS_{RW,}$

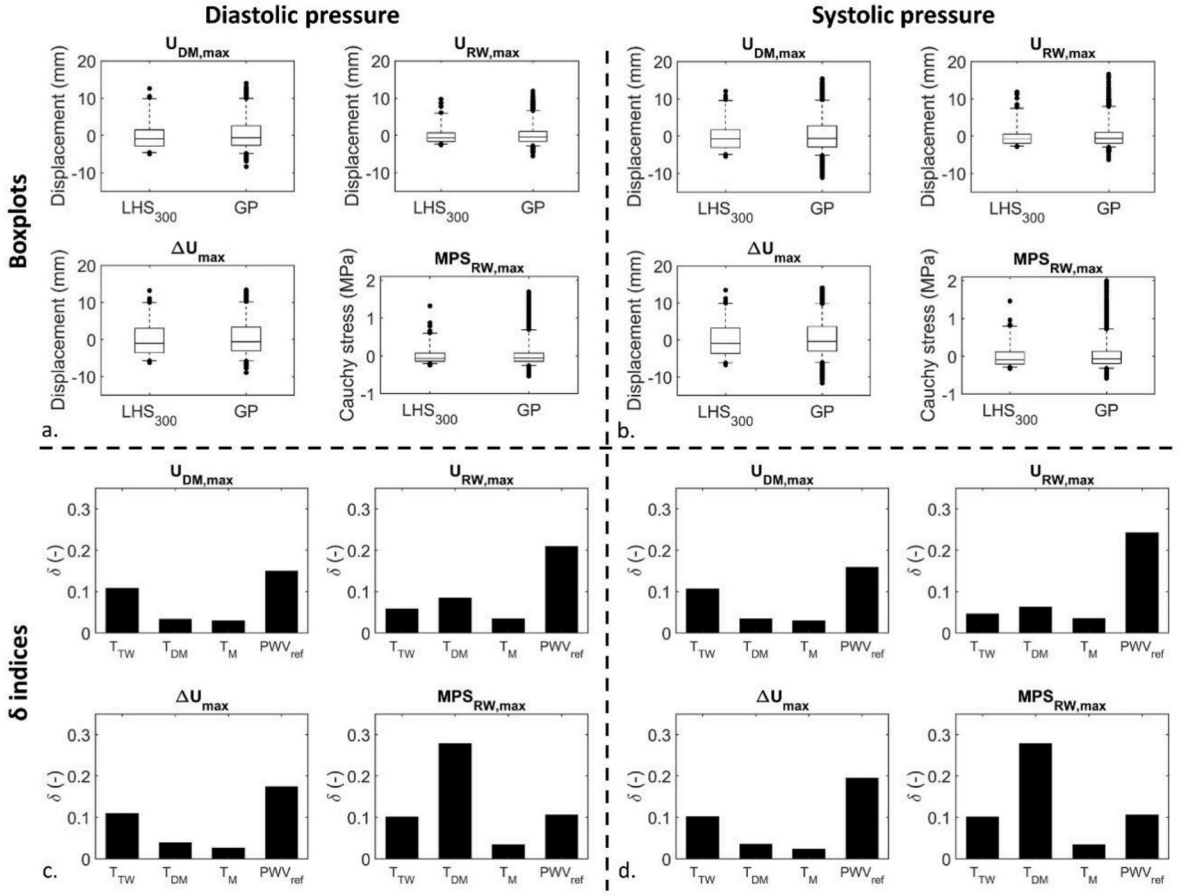


**Fig. 7.** The resulting (a, b) boxplots based on the $LHS_{300}$ and the Gaussian process (GP) with the corresponding (c, d) δ indices at (a, c) diastolic (80 mmHg) and (b, d) systolic (120 mmHg) pressure. The output parameters $U_{DM,max}$, $U_{RW,max}$, $\Delta U_{max}$ and $MPS_{RW,max}$ indicate the maximal displacement of the dissected membrane, the maximal displacement of the remaining wall, the maximal distance between the dissected membrane and remaining wall and the maximal principal Cauchy stress at the maximal displacement of the remaining wall. The whiskers of the boxplots show the central 95% of the output values, i.e. the values used for the δ moment-independent analysis.

$_{max}$ at diastolic and systolic pressure (appendix B). This translates into RMSE values between 10% and 22% of the corresponding median values, based on the $LHS_{300}$ results, for $U_{DM,max}$ and $\Delta U_{max}$, while errors from 30% to 48% are obtained for $MPS_{RW,max}$ and $U_{RW,max}$. The output distribution obtained as result of the Gaussian process and the $LHS_{10,000}$ was compared to the one based on the finite element analyses of $LHS_{300}$, as indicated in Fig. 7(a, b). In particular, the central 95% of the output distribution was found to be comparable.

#### 3.3.2. Delta moment-independent analysis

The δ indices at diastolic and systolic pressure, resulting from the application of the Gaussian process on the performed $LHS_{10,000}$ sampling are shown in Fig. 7(c, d) and appendix C. The thickness input parameters lead to $\delta \leq 0.11$ for $U_{DM,max}$, $U_{RW,max}$ and $\Delta U_{max}$. While $T_{TW}$ is the thickness parameter that affects the displacement output distribution the most for $U_{DM,max}$ and $\Delta U_{max}$, $T_{DM}$ and $T_M$ induce a minor shift in output distribution ($0.02 \leq \delta \leq 0.08$). For $U_{RW,max}$, all thickness parameters resulted in $\delta \leq 0.08$, with $T_{DM}$ being slightly more important compared to $T_{TW}$ and $T_M$. The input parameter with the highest importance for all displacement output parameters is $PWV_{ref}$, with $0.15 \leq \delta \leq 0.24$. On contrary, for $MPS_{RW,max}$, the largest impact is attributed to $T_{DM}$ with $0.28 \leq \delta \leq 0.30$. The distribution is to a lesser extent affected by $T_{TW}$ and $PWV_{ref}$ ($0.10 \leq \delta \leq 0.11$) and $T_M$ ($\delta = 0.03$).

### 3.4. Additional sources of uncertainty

#### 3.4.1. Pressure gradient

The absolute values of the median displacement differences, with respect to the corresponding results without pressure gradient, are larger at diastolic than at systolic pressure, but remain below 1.0 mm (Table 3). In diastole, the magnitude of $U_{DM,max}$ and $\Delta U_{max}$ increases, while a decreasing displacement magnitude is found for $U_{RW,max}$ by adding the pressure gradient. In systole, the opposite effect is observed. The impact of the pressure gradient on $MPS_{RW,max}$ is negligible with a median difference below 0.001 MPa. The width of the resulting min-max interval varies between 92% and 103% of the corresponding interval obtained without pressure gradient, again indicating a limited effect. Taking the difference between $U_{DM,max}$ of the corresponding diastolic and systolic configurations, with inclusion of the pressure gradient, results in estimated dissected membrane movements of 0.01 mm–1.71 mm.

#### 3.4.2. Axial dissection length

The slice model results in median displacement differences up to 2.08 mm and indicates an increasing displacement in $U_{DM,max}$ and $\Delta U_{max}$, while $U_{RW,max}$ decreases (Table 3). Similarly, the width of the min-max intervals increases for $U_{DM,max}$ and $\Delta U_{max}$ with up to 53%, compared to the idealized dissection model results, whereas a 55% decrease in interval width is observed for $U_{RW,max}$. For $MPS_{RW,max}$, the median difference is limited to an increase of 0.03 MPa, while the width of the min-max interval increases with 29%.

## 4. Discussion

### 4.1. Dissected wall model framework

A computational framework for an idealized dissected two-layered aortic wall was developed. Although an idealized wall geometry is applied, it contains the main characteristics of an aortic dissection, i.e. the false lumen and the tears. Moreover, it includes anisotropic hyperelastic material behavior as well as residual stresses. Despite the fact that the cause and progression of the dissection is discarded in this study, the current framework allows for an, at least partially, physiological representation of an acute aortic dissection. Indeed, the shape of the true and false lumen is not predetermined, but is created based on the release of the residual stresses in the dissected membrane and the application of the true and false lumen pressure. Consequently, a realistic deformation is ensured, without requiring detailed knowledge on the exact cause of the dissection.

Based on the implemented framework, 237 out of the 300 considered samples ($LHS_{300}$) fulfilled the FEA convergence criteria (8% of the 300 samples excluded) and resulted in $g_{e,circ} \geq 1.0$ throughout the wall for the sample geometry (13% of the 300 samples excluded). As 79% of the $LHS_{300}$ samples leads to useful results, the framework in itself was considered to be quite robust. The finite element analysis in itself was even more robust with a success rate of 90%. Indeed, after excluding the samples based on $g_{e,circ}$, 90% of the simulations lead to a converged result.

While not contributing to the uncertainty quantification, the position of the excluded samples in the input parameter space provides interesting information. In this respect, the histograms and 2-dimensional projections of the input parameters of the samples were considered. The histograms of the samples that did not fulfill the finite element analysis convergence criteria were quite uniformly distributed for most input parameters, similarly to the applied distributions. Nevertheless, nearly all non-converging samples (21 of the 25 samples) were situated in the lower half of the $T_w$ range. On the contrary, the excluded samples with $g_{e,circ} < 1.0$ were mainly (37 of the 38 samples) situated in the upper half of the $T_w$ range. Moreover, most of these samples (34 of the 38 samples) were related to a $PWV_{ref}$ between 7.0 and 10.0 m/s. While these samples were excluded due to a non-physiological $g_{e,circ}$, it is noteworthy that this exclusion relates to the choice of reference cylinder, rather than to non-physiological parameter combinations. In the 2-dimensional projections of the converged samples, the exclusion of samples results in two minor (in the $PWV_{ref}$-$T_M$ and the $PWV_{ref}$-$T_{DM}$ projection) and one larger, though still limited, unexplored regions. The

**Table 3**
The effect of altering the pressure gradient or dissection length in 10 configurations, at diastolic (80 mmHg) and systolic (120 mmHg) pressure. The median value of the difference between $U_{DM,max}$, $U_{RW,max}$, $\Delta U_{max}$ and $MPS_{RW,max}$ in the adapted and the original idealized dissected wall framework is presented. The width of the min-max range obtained based on the 10 configurations is included as well and is presented relative to the min-max interval of the counterpart results of the idealized dissected model framework.

| | Pressure gradient | | Dissection length | |
|---|---|---|---|---|
| Output | Median difference | Min-max width (%) | Median difference | Min-max width (%) |
| **Diastole** | | | | |
| $U_{DM,max}$ (mm) | 0.69 | 103 | 1.76 | 153 |
| $U_{RW,max}$ (mm) | −0.11 | 97 | −0.80 | 45 |
| $\Delta U_{max}$ (mm) | 0.39 | 92 | 0.60 | 106 |
| $MPS_{RW,max}$ (MPa) | −0.0004 | 99 | 0.02 | 122 |
| **Systole** | | | | |
| $U_{DM,max}$ (mm) | −0.32 | 94 | 2.08 | 153 |
| $U_{RW,max}$ (mm) | 0.07 | 101 | −0.86 | 46 |
| $\Delta U_{max}$ (mm) | −0.32 | 99 | 0.72 | 108 |
| $MPS_{RW,max}$ (MPa) | 0.0007 | 100 | 0.03 | 129 |

larger unexplored region is situated at a $T_w > 2.16$ mm combined with a $PWV_{ref}$ in the range of 8.4–9.8 m/s. As only one noticeable unexplored region is identified, the impact of the non-converging and excluded samples on the overall uncertainty analysis is expected to be limited.

### 4.2. Global uncertainty quantification based on finite element analyses

Based on the developed model framework of the dissected wall and the performed finite element analyses, the overall uncertainty on the considered deformation and stresses, as a consequence of uncertain thickness and stiffness parameters, was estimated at diastolic and systolic pressure levels. Despite slight differences in the absolute median values, the magnitude of the global min-max and IQ uncertainty ranges was very similar at diastolic and systolic pressure, especially when considering the large variety in the input parameter space (Fig. 6 and Table 2). It might, therefore, be sufficient to study the uncertainty based on one loading state for a quasi-static model.

The IQ uncertainty ranges were maximally 6.88 mm and 0.32 MPa for the displacement and stress output parameters, respectively, whereas the min-max ranges showed uncertainty intervals up to 20.22 mm and 1.79 MPa, which is in particular induced by the large variation in the 4$^{th}$ quartile for all output parameters (Fig. 6 and Table 2). The min-max interval width of $U_{DM,max}$ can be interpreted as the maximal error in the predicted true lumen diameter decrease, which is linked to the risk of malperfusion. $U_{RW,max}$ can be interpreted as the maximal error in the total diameter increase, which is currently used as a clinical decision criterion. At diastolic pressure, the current study estimates model output errors up to 64% for the decrease in true lumen diameter and up to 45% for the increase in total diameter, relative to the diameter of the healthy descending aorta. Note that this interpretation implicitly assumes that axial bending of the dissected wall is negligible. Although these extreme values are expected to occur rarely, it is of major importance to acknowledge their presence, as their exclusion could result in an under- or overestimation of the malperfusion and rupture risk and, consequently, in inappropriate clinical decisions.

Despite this increased insight, the model framework is expected to underestimate the true uncertainty. Indeed, the direct coupling of $PWV_{ref}$ to a set of GOH parameters assumes that the pulse wave velocity is measured with high accuracy and fully represents the material behavior. However, some measurement errors might be expected and the pulse wave velocity is mainly a stiffness measure of the circumferential behavior. Therefore, pulse wave velocity is rather a guide than an exact measure to obtain proper material parameters (Gheysen et al., 2023). The link between the $PWV_{ref}$ and the GOH parameter set is, consequently, not straightforward and includes additional uncertainty, which was not accounted for in the main uncertainty analysis. The impact of the use of $PWV_{ref}$ as material parameter is considered in appendix D and reveals remarkable variations, in particular for the wall deformation, for slight changes in $PWV_{ref}$, while applying constant thickness parameters. Although this additional uncertainty is not accounted for in the main analysis, it does not invalidate the obtained results, but indicates that the quantified uncertainty must be considered as a lower boundary as the tissue-specific GOH parameter are often unknown.

### 4.3. Parameter-specific uncertainty quantification based on surrogate models

The δ moment-independent analysis shows the importance of each individual input parameter on the output distribution, thus, indicating which information is an essential prerequisite for the development of reliable predictive models (Fig. 7 and appendix C). $T_M$ was found to have a negligible effect on all considered output parameters, and is, consequently, not expected to largely influence the predicted wall deformation and stress. The impact of the other thickness parameters depends on the considered output parameter. On the one hand, $T_{TW}$ affects the output distribution of $MPS_{RW,max}$ and the displacement parameters involving the dissected membrane, i.e. $U_{DM,max}$ and $\Delta U_{max}$, to some extent, but has little effect on the output distribution of $U_{RW,max}$. On the other hand, knowing the true value for $T_{DM}$ is of minor importance for all displacement output parameters, but leads to the largest impact on the output distribution of $MPS_{RW,max}$. For the material stiffness, represented by $PWV_{ref}$, the opposite effect is noticed. Indeed, uncertainty on $PWV_{ref}$ yields the strongest impact on the displacement output distributions, while its influence on the $MPS_{RW,max}$ distribution remains moderate. These observations suggest that, in particular, patient-specific knowledge on the global material stiffness and the relative thickness of the dissected membrane is essential when one is interested in the respective prediction of the deformation and peak wall stress in aortic dissections, which is in line with basic mechanical insights.

The actual values of the obtained δ indices might, however, be affected by the considered input parameter space and the Gaussian process regression, which depends on the specific training and test set. To assess the added value of the trained Gaussian process on the parameter-specific uncertainty quantification, the indices obtained for the $LHS_{10,000}$ are compared to those directly obtained from the $LHS_{300}$ together with the corresponding 95% confidence intervals on the δ indices. As indicated in appendix C, most general trends are, although less pronounced, similar for both sets of δ indices, which enhances the confidence in the reported indices. Nevertheless, the confidence intervals of the indices largely decrease with an increasing number of samples, which confirms the added value of training a surrogate model based on the finite element results to perform the parameter-specific sensitivity analysis. In addition, the robustness of the obtained δ indices, based on $LHS_{10,000}$, is tested with respect to the sampling based on the trained Gaussian process (appendix C). Therefore, the same $LHS_{10,000}$ is resampled with the same Gaussian process, which yields very similar δ indices. It might, therefore, be assumed that the indices are the result of the intrinsic trends of the Gaussian process, rather than being a result of a specific sampling and, thus, the Gaussian process uncertainty.

In the presented methodology a Latin hypercube sampling was utilized to train a Gaussian process regression. Alternative approaches have been considered before. Brunet et al. (2021), for example, considered two values for each input parameter of interest, performed a full factorial design and a linear regression, including interaction effects, based on a least squares method. When applying this methodology to the presented case, the number of samples can be decreased to 16 (i.e. $2^4$). However, a linear relation between the input and output parameters cannot be guaranteed in the considered case. Using linear regression would, therefore, potentially exclude nonlinear effects *a priori* and, thus, result in a relation that strongly depends on the sample selection when only considering two values per parameter. Moreover, by training a linear rather than a Gaussian process regression, the remaining surrogate model uncertainty is not accounted for. A full factorial design in itself can be applied as sampling strategy instead of the Latin hypercube sampling, provided that it densely covers the input parameter space. However, it would result in a much larger amount of samples for the same number of values per parameter (i.e. $300^4$) and strongly increase the computational cost.

### 4.4. Physiological relevance of idealized dissected framework

While mean dissected membrane movements of 1.7–5.5 mm in the descending aorta throughout the cardiac cycle have been measured *in vivo*, the idealized dissected wall model resulted in dissected membrane movements between diastolic and systolic pressure from 0.01 mm to 1.71 mm when adding a physiological pressure difference of 3 mmHg between the true and false lumen (Bäumler et al., 2020; Ganten et al., 2009; Pirola et al., 2019; Yang et al., 2014). Despite differences in the methodology to measure the dissected membrane movement over the cardiac cycle, due to the different nature of the computational and

experimental results, this indicates that the model framework results in displacements which are in the same order of magnitude, but smaller compared to the *in vivo* measurements.

It is speculated that at least part of the remaining difference between the modelled and measured dissected membrane movement is related to the limited axial dissection length of 40 mm. Indeed, physiological dissections often extend from the left subclavian artery until the abdominal aorta (Bäumler et al., 2020; Ganten et al., 2009). The slice model represents an infinitely long dissection and results at systolic pressure in a median $U_{DM,max}$ deviation of 33%, relative to the median of the corresponding idealized dissected wall samples (Table 3 and supplementary material). This deviation is 3 times higher than the median difference obtained by the addition of the pressure gradient. This suggests that the axial dissection length impacts $U_{DM,max}$ to a larger extent than the inclusion of the pressure gradient. It is, therefore, expected that an increased axial dissection length will enhance the dissected membrane movement during the cardiac cycle.

In addition, the similarity between the wall stress pattern of the current model and the idealized dissection model of Rolf-Pissarczyk et al. (2021) supports that the limited dissected membrane movement results from the short dissection length rather than from physiological limitations of the presented model framework. Indeed, in both models, local concentrations in maximal principal stress were obtained in the remaining wall at the location of separation with the dissected membrane, while the dissected membrane was found to contain negligible stresses (Fig. 4 and appendix A).

Despite the differences in absolute values compared to physiological measurements, it must be emphasized that the current study aims to quantify the uncertainty. On the one hand, adding the pressure gradient over the dissected membrane leads to slight deviations of 0%–8% in the width of the min-max interval (Table 3). On the other hand, the slice model resulted for $U_{RW,max}$ in an interval that was 55% smaller, while 53% larger ranges were obtained for $U_{DM,max}$ (Table 3). Despite the fact that using a limited axial dissection length might underestimate the expected uncertainty, in particular for $U_{DM,max}$, it should be noted that the slice model also represents an upper boundary rather than a physiological case. Moreover, the obtained uncertainty ranges of the additional finite element analyses, still fall within the reported min-max interval based on the complete $LHS_{300}$. Therefore, the use of an idealized model framework is not expected to largely compromise the uncertainty quantification.

### 4.5. Lessons learned from surrogate modelling

In the current study, it was opted to train a Gaussian process as surrogate model, rather than a neural network. Indeed, neural networks provide a deterministic result, which is reasonable when large datasets are available and, consequently, accurate networks can be trained. Due to the computational cost, the sample number for the finite element analyses in this study is limited to 300, thus the samples do not cover the input parameter space very densely. The fact that a Gaussian process accounts for the remaining uncertainty in the surrogate model, therefore, enhances the reliability of the results of the δ moment-independent analysis. Note that the 5% extreme output values were, nevertheless, excluded to find a trade-off between the inclusion of the intrinsic uncertainty, which increases the reliability, and the exclusion of potentially unphysiological results, which might negatively affect the reliability.

To train the Gaussian processes, the $PWV_{ref}$ is replaced by the 7 corresponding GOH material parameters (section 2.1.2) and the resulting sample $g_{e,circ}$ to obtain a sufficiently low RMSE ($\leq$1.0 mm) for the displacement output parameters. Although this target is not reached for the Gaussian process of $U_{DM,max}$ and $U_{RW,max}$ at systolic pressure, this methodology best approaches the RMSE requirement. Indeed, Gaussian processes trained with less input parameters result in insufficiently accurate surrogate models (appendix B). Note that the 7 GOH parameters and the sample $g_{e,circ}$ are also required as input to the finite element model, which justifies the obtained Gaussian processes as it follows the same steps as the finite element analysis.

Moreover, it is worth mentioning that the reported RMSE values provide an indication, rather than a general statement, as a different Latin hypercube sampling for the training and/or test set results in a different Gaussian process and/or corresponding RMSE. The effect of a different test set is assessed by generating a control test sampling $LHS_{30,control}$ and subjecting it to the trained Gaussian processes. Compared to the $LHS_{30}$, the $LHS_{30,control}$ yields lower RMSE values for most Gaussian processes and fulfills the required RMSE threshold of 1.0 mm for all displacement output parameters. Although these results enhance the reliability of the Gaussian processes, it mainly illustrates that caution should be taken when evaluating a Gaussian process on a single RMSE value.

Besides, one could argue whether a RMSE threshold of 1.0 mm, based on a representative resolution of clinical CT scans, is sufficiently strict for the developed surrogate models. Indeed, as the idealized deformation might underestimate the physiological one, the absolute RMSE might also be an underestimation of the expected physiological deviation, when assuming that the relative RMSE remains constant.

In this respect, it is important to emphasize that the current aim of the trained Gaussian processes is to provide insight into the uncertainty, rather than providing a clinically applicable surrogate model. As the overall output distribution obtained from the Gaussian processes was similar to those of the finite element analyses, in particular for values within the central 95% of the output distribution, the applicability of the current methodology for uncertainty quantification is supported.

Nevertheless, the technique might be promising for outcome prediction and uncertainty quantification in a clinical setting too, as it yields real-time probabilistic predictions. Indeed, accurate Gaussian processes of the false lumen size, i.e. $\Delta U_{max}$, could for example assist in deriving proper GOH parameter combinations from the deformation of the dissection, which can be observed in clinical CT scans, and inverse Bayesian inference. However, this would require more data and/or knowledge as a prerequisite to further enhance the accuracy of the Gaussian process.

### 4.6. Limitations

Although aimed at uncertainty quantification, the current framework inevitably contains assumptions as well. The studied geometry was fixed and only one inner diameter and one configuration for the tears and false lumen was implemented. Moreover, the wall thicknesses and the residual stresses were assumed to be homogeneous along the circumferential and axial directions, which does not correspond to the physiological reality (Bersi et al., 2016; Sokolis, 2020). Besides, the idealized geometry deviates from a patient-specific one, not only in terms of pressure difference and dissection length as discussed above, but also in terms of geometrical complexity, as no side branches, tortuosity or external soft tissue support was included. These aspects might result in an under- or overestimation of the deformation and wall stress of the remaining wall and dissected membrane (Ferraro et al., 2018; Georgakarakos et al., 2010). Although including these complexities might further advance the translation of the obtained uncertainty results to the clinical practice in absolute terms, it was opted to use an idealized model with the most important characteristics to allow the use of a systematic approach to unravel the effect of the unknown wall thicknesses and stiffness. Moreover, the added value of the model framework is situated in the increased insight into the uncertainty quantification, on a global as well as on a parameter-specific basis.

Regarding the material behavior, the collagen fiber dispersion was considered as axisymmetric, while differences between the in- and out-of-plane dispersion have been observed (Niestrawska et al., 2016; Schriefl et al., 2012). A material model that accounts for dispersion asymmetry, such as proposed by Holzapfel et al. (2015), is expected to

more accurately approach the *in vivo* aortic wall mechanics, which was confirmed by an improved fitting with experimental data (Dal et al., 2023). However, no radial tensile stresses were observed in the idealized dissection model, which implies that radial collagen fibers will not contribute to the overall stress state as they are not recruited. An asymmetric dispersion model will, hence, only differ from the implemented model in its increased amount of fibers close to or in the local axial-circumferential plane. While this deviation might affect the absolute wall stress and deformation, as indicated by Niestrawska et al. (2018), the overall material behavior remains similar, which suggests a limited impact on the uncertainty. Moreover, the properties of healthy aortic wall tissue were used as a starting point. Consequently, the developed framework is assumed to represent an acute type B aortic dissection. Indeed, to model a chronic type B aortic dissection, growth and remodeling should be applied to represent the stiffening of the membrane after dissection (Peterss et al., 2016). In this respect, the quantified uncertainty and the parameter-specific importance is only valid in the situation of an acute dissection. Indeed, the addition of growth and remodeling might result in a different impact of the considered thickness and stiffness parameters on the long-term deformation and stress of the dissected wall.

Moreover, the cause of dissection might be related to altered wall properties. Indeed, type B dissections are associated with degradation in the medial layer which is, amongst others, characterized by fragmented elastic fibers, a reduced elastin fraction and the accumulation of glycosaminoglycans in pools (Humphrey, 2013; Wu et al., 2013). Therefore, it is possible that the included state-of-the-art material model, with integration of the anisotropic behavior and constituent-specific deposition stretches, is not fully representative for the dissected wall tissue. However, Rolf-Pissarczyk et al. (2021) implemented a constitutive law to include the radial elastic fiber degradation in between the medial elastic lamellae, but did not see a clear effect of the adapted material model in their model of the dissected wall. Nevertheless, adaptations in circumferential and longitudinal stiffness and strength as well as changes in collagen content of the acute dissected wall, compared to non-dissected aortic walls, have been observed (Borges et al., 2008; Deplano et al., 2019; Manopoulos et al., 2018; Sherifova and Holzapfel, 2019; Yamada et al., 2015). These effects were not considered by Rolf-Pissarczyk et al. (2021) and might affect the resulting wall stress and deformation of the model. As the considered material parameter combinations cover a large range of pulse wave velocities in health and disease, the impact of these differences between the material of the dissected and healthy aortic wall on the quantified uncertainty is expected to remain limited.

## 5. Conclusion

In summary, a robust idealized dissected wall framework was developed that included an anisotropic hyperelastic material behavior as well as residual stresses. It enabled the prediction of the acute wall deformation in a physiology-inspired manner. With this framework, the effect of uncertainty related to wall thickness and stiffness parameters on the wall deformation and stress was assessed. Large ranges of potential wall deformations and stresses were identified by the global uncertainty analysis, in particular when including the extreme outcomes, which might strongly affect the clinical decision. The parameter-specific uncertainty analysis suggested that the modelled material stiffness strongly affects the dissected wall deformation, while the relative dissected membrane thickness was the most important determinant for the wall stress. The large uncertainty ranges and the varying impact of, often unknown, wall stiffness and thickness parameters emphasize the need for caution when interpreting the outcome of dissected wall models. Moreover, it supports the use of probabilistic rather than deterministic predictions for clinical decision making in aortic dissections.

## CRediT authorship contribution statement

**Lise Gheysen:** Writing – original draft, Visualization, Software, Methodology, Investigation, Funding acquisition, Formal analysis, Conceptualization. **Lauranne Maes:** Writing – review & editing, Software, Methodology, Funding acquisition. **Annette Caenen:** Writing – review & editing, Supervision, Software. **Patrick Segers:** Writing – review & editing, Supervision, Methodology, Funding acquisition, Conceptualization. **Mathias Peirlinck:** Writing – review & editing, Supervision, Software, Methodology, Conceptualization. **Nele Famaey:** Writing – review & editing, Supervision, Methodology, Funding acquisition, Conceptualization.

## Declaration of competing interest

The authors declare that they have no known competing financial interests or personal relationships that could have appeared to influence the work reported in this paper.

## Data availability

The scripts required to reproduce the presented results are published on Zenodo with DOI 10.5281/zenodo.8372127 under the Creative Commons Attribution 4.0 International license.

## Acknowledgements

We are grateful to Dr. Markus Wagenhäuser (University Hospital of Düsseldorf, Germany) for the data collection of the CT scans.

Funding This work was supported by the Foundation Research Flanders (FWO) [grant numbers 1S48920N, 11A6519N and G029819N].

## Appendix A. Examples of maximal principal stress patterns

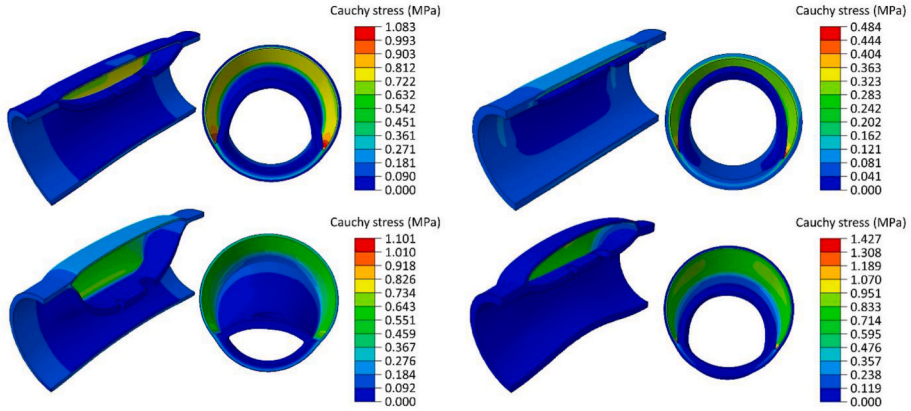


**Fig. A1.** Overview of the maximal principal wall stress on the deformed configuration at diastolic pressure (80 mmHg) for 4 examples of the $LHS_{300}$, i.e. those corresponding to the first row of Fig. 4. For each example, an axial and a cross-sectional cut is shown, together with the corresponding color scale.

## Appendix B. RMSE of Gaussian processes

### B.1. $LHS_{30}$ and $LHS_{30,control}$

**Table B1**
Overview of the RMSE of the trained Gaussian process per output parameter at diastolic (80 mmHg) and systolic (120 mmHg) pressure based on the test set $LHS_{30}$ and the control test set $LHS_{30,control}$. The RMSE are presented as absolute values as well as relative to the median $LHS_{300}$ value.

| | Diastole | | Systole | |
|---|---|---|---|---|
| RMSE | $LHS_{30}$ | $LHS_{30,control}$ | $LHS_{30}$ | $LHS_{30,control}$ |
| $U_{DM,max}$ (mm) | 0.94 (16%) | 0.71 (12%) | 1.43 (22%) | 0.83 (13%) |
| $U_{RW,max}$ (mm) | 0.73 (33%) | 0.83 (38%) | 1.26 (48%) | 0.96 (36%) |
| $\Delta U_{max}$ (mm) | 0.77 (10%) | 0.60 (8%) | 0.88 (10%) | 0.74 (9%) |
| $MPS_{RW,max}$ (MPa) | 0.075 (29%) | 0.032 (12%) | 0.120 (30%) | 0.054 (14%) |

### *B.2. Gaussian processes with different number of input parameters*

**Table B2**
Overview of the RMSE of the Gaussian process based on 4 ($GP_4$, i.e. based on the 4 independent input thickness and stiffness parameters $T_{TW}$, $T_M$, $T_{DM}$ and $PWV_{ref}$ only), 10 ($GP_{10}$, i.e. with exclusion of $g_{e,circ}$ as input parameter) and 11 ($GP_{11}$, i.e. the Gaussian process used in the study) input parameters at diastolic (80 mmHg) and systolic (120 mmHg) pressure. The RMSE are presented as absolute values as well as with respect to the median $LHS_{300}$ value.

| | Diastole | | | Systole | | |
|---|---|---|---|---|---|---|
| RMSE | $GP_4$ | $GP_{10}$ | $GP_{11}$ | $GP_4$ | $GP_{10}$ | $GP_{11}$ |
| $U_{DM,max}$ (mm) | 3.65 (61%) | 1.54 (26%) | 0.94 (16%) | 3.69 (57%) | 2.19 (34%) | 1.43 (22%) |
| $U_{RW,max}$ (mm) | 2.08 (95%) | 0.72 (33%) | 0.73 (33%) | 3.23 (122%) | 0.99 (37%) | 1.26 (48%) |
| $\Delta U_{max}$ (mm) | 4.05 (52%) | 1.50 (19%) | 0.77 (10%) | 3.91 (45%) | 1.65 (19%) | 0.88 (10%) |
| $MPS_{RW,max}$ (MPa) | 0.188 (73%) | 0.089 (34%) | 0.075 (29%) | 0.210 (53%) | 0.127 (32%) | 0.120 (30%) |

## Appendix C. Comparison of δ indices

### C.1. Comparison of δ indices of $LHS_{300}$ and $LHS_{10,000}$

**Table C1**
Overview of δ indices and the corresponding 95% confidence interval ($\delta_{conf}$) as a result of the δ moment-independent analysis for output parameters $U_{DM,max}$, $U_{RW,max}$, $\Delta U_{max}$ and $MPS_{RW,max}$ based on the results of $LHS_{300}$ and the central 95% of the output of $LHS_{10,000}$ at diastolic (80 mmHg) and systolic (120 mmHg) pressure.

| Input parameter | | $U_{DM,max}$ | | $U_{RW,max}$ | | $\Delta U_{max}$ | | $MPS_{RW}$ | | |
|---|---|---|---|---|---|---|---|---|---|---|
| | | δ | $\delta_{conf}$ | δ | $\delta_{conf}$ | δ | $\delta_{conf}$ | δ | $\delta_{conf}$ | |
| **Diastole** | | | | | | | | | | |
| $T_{TW}$ | $LHS_{300}$ | 0.085 | 0.037 | 0.028 | 0.028 | 0.076 | 0.039 | 0.099 | 0.041 | |
| | $LHS_{10,000}$ | 0.107 | 0.006 | 0.057 | 0.007 | 0.109 | 0.007 | 0.101 | 0.008 | |
| $T_{DM}$ | $LHS_{300}$ | 0.044 | 0.033 | 0.091 | 0.041 | 0.045 | 0.034 | 0.198 | 0.060 | |
| | $LHS_{10,000}$ | 0.033 | 0.005 | 0.084 | 0.008 | 0.039 | 0.006 | 0.278 | 0.008 | |

(*continued on next page*)

**Table C1** (*continued*)

| Input parameter | $U_{DM,max}$ | | $U_{RW,max}$ | | $\Delta U_{max}$ | | $MPS_{RW}$ | | |
|---|---|---|---|---|---|---|---|---|---|
| | δ | $\delta_{conf}$ | δ | $\delta_{conf}$ | δ | $\delta_{conf}$ | δ | $\delta_{conf}$ | |
| $T_M$ | $LHS_{300}$ | 0.021 | 0.030 | 0.039 | 0.032 | 0.009 | 0.027 | 0.071 | 0.031 |
| | $LHS_{10,000}$ | 0.029 | 0.005 | 0.034 | 0.005 | 0.026 | 0.005 | 0.033 | 0.005 |
| $PWV_{ref}$ | $LHS_{300}$ | 0.045 | 0.032 | 0.131 | 0.047 | 0.075 | 0.042 | 0.132 | 0.033 |
| | $LHS_{10,000}$ | 0.150 | 0.009 | 0.209 | 0.010 | 0.173 | 0.011 | 0.106 | 0.008 |
| **Systole** | | | | | | | | | |
| $T_{TW}$ | $LHS_{300}$ | 0.091 | 0.037 | 0.039 | 0.025 | 0.080 | 0.040 | 0.099 | 0.036 |
| | $LHS_{10,000}$ | 0.106 | 0.007 | 0.046 | 0.005 | 0.102 | 0.007 | 0.103 | 0.007 |
| $T_{DM}$ | $LHS_{300}$ | 0.051 | 0.034 | 0.077 | 0.040 | 0.050 | 0.037 | 0.224 | 0.053 |
| | $LHS_{10,000}$ | 0.034 | 0.006 | 0.062 | 0.007 | 0.035 | 0.007 | 0.303 | 0.009 |
| $T_M$ | $LHS_{300}$ | 0.025 | 0.029 | 0.053 | 0.027 | 0.010 | 0.029 | 0.063 | 0.033 |
| | $LHS_{10,000}$ | 0.029 | 0.005 | 0.034 | 0.005 | 0.024 | 0.005 | 0.028 | 0.005 |
| $PWV_{ref}$ | $LHS_{300}$ | 0.040 | 0.033 | 0.117 | 0.036 | 0.093 | 0.042 | 0.117 | 0.031 |
| | $LHS_{10,000}$ | 0.159 | 0.010 | 0.242 | 0.011 | 0.195 | 0.012 | 0.095 | 0.008 |

### *C.2. Comparison of δ indices of $LHS_{10,000}$ and a resampling*

**Table C2**
Overview of δ indices and the corresponding 95% confidence interval as a result of the δ moment-independent analysis for output parameters $U_{DM,max}$, $U_{RW,max}$, $\Delta U_{max}$ and $MPS_{RW,max}$ based on the results of the central 95% of the output of $LHS_{10,000}$ and a resampling of the same $LHS_{10,000}$ with the same Gaussian process, indicated as $LHS_{10,000,resample}$, at diastolic (80 mmHg) and systolic (120 mmHg) pressure.

| Input parameter | $U_{DM,max}$ | | | $U_{RW,max}$ | | $\Delta U_{max}$ | | $MPS_{RW,max}$ | |
|---|---|---|---|---|---|---|---|---|---|
| | δ | $\delta_{conf}$ | δ | $\delta_{conf}$ | δ | $\delta_{conf}$ | δ | $\delta_{conf}$ | |
| **Diastole** | | | | | | | | | |
| $T_{TW}$ | $LHS_{10,000,resample}$ | 0.096 | 0.007 | 0.067 | 0.007 | 0.111 | 0.006 | 0.096 | 0.006 |
| | $LHS_{10,000}$ | 0.107 | 0.006 | 0.057 | 0.007 | 0.109 | 0.007 | 0.101 | 0.008 |
| $T_{DM}$ | $LHS_{10,000,resample}$ | 0.034 | 0.006 | 0.084 | 0.008 | 0.040 | 0.006 | 0.305 | 0.008 |
| | $LHS_{10,000}$ | 0.033 | 0.005 | 0.084 | 0.008 | 0.039 | 0.006 | 0.278 | 0.008 |
| $T_M$ | $LHS_{10,000,resample}$ | 0.032 | 0.005 | 0.034 | 0.005 | 0.025 | 0.005 | 0.036 | 0.005 |
| | $LHS_{10,000}$ | 0.029 | 0.005 | 0.034 | 0.005 | 0.026 | 0.005 | 0.033 | 0.005 |
| $PWV_{ref}$ | $LHS_{10,000,resample}$ | 0.152 | 0.009 | 0.214 | 0.009 | 0.166 | 0.010 | 0.105 | 0.008 |
| | $LHS_{10,000}$ | 0.150 | 0.009 | 0.209 | 0.010 | 0.173 | 0.011 | 0.106 | 0.008 |
| **Systole** | | | | | | | | | |
| $T_{TW}$ | $LHS_{10,000,resample}$ | 0.100 | 0.007 | 0.046 | 0.005 | 0.119 | 0.007 | 0.101 | 0.008 |
| | $LHS_{10,000}$ | 0.106 | 0.007 | 0.046 | 0.005 | 0.102 | 0.007 | 0.103 | 0.007 |
| $T_{DM}$ | $LHS_{10,000,resample}$ | 0.036 | 0.005 | 0.054 | 0.006 | 0.034 | 0.005 | 0.299 | 0.009 |
| | $LHS_{10,000}$ | 0.034 | 0.006 | 0.062 | 0.007 | 0.035 | 0.007 | 0.303 | 0.009 |
| $T_M$ | $LHS_{10,000,resample}$ | 0.032 | 0.006 | 0.038 | 0.005 | 0.027 | 0.006 | 0.035 | 0.005 |
| | $LHS_{10,000}$ | 0.029 | 0.005 | 0.034 | 0.005 | 0.024 | 0.005 | 0.028 | 0.005 |
| $PWV_{ref}$ | $LHS_{10,000,resample}$ | 0.157 | 0.010 | 0.234 | 0.012 | 0.183 | 0.009 | 0.094 | 0.008 |
| | $LHS_{10,000}$ | 0.159 | 0.010 | 0.242 | 0.011 | 0.195 | 0.012 | 0.095 | 0.008 |

## Appendix D. Impact of direct coupling between the $PWV_{ref}$ and GOH parameters

### *D.1. Methods*

In a previous study, it was found that the pulse wave velocity can guide the selection of GOH parameters, but does not provide a direct relation (Gheysen et al., 2023). In the current framework, this direct link was, nevertheless, assumed in order to facilitate the use of the Latin hypercube sampling. To consider the effect of this assumption, the reference geometry (section 2.1.3.) was simulated with the 10 GOH parameter combinations that most closely corresponded to a $PWV_{ref}$ of 5 m/s. The median difference, with respect to the results that would be obtained with the idealized dissected wall framework, was determined. Note that one of the 10 analyses, by definition, corresponded to the result of the presented framework. The uncertainty induced by coupling the pulse wave velocity to other GOH parameter combinations was assessed as the resulting min-max range.

### *D.2. Results*

The 10 samples with the $PWV_{ref}$ closest to 5 m/s maximally deviated 0.0017 m/s from this target. While the median difference of $MPS_{RW,max}$ shows a maximal decrease in magnitude of 0.005 MPa, median increases in magnitude up to 4.97 mm, with respect to the initial framework, are obtained for the displacement output parameters (table D1). The width of the resulting min-max ranges was close to 50% of the min-max interval of the $LHS_{300}$ for the displacement parameters. Smaller min-max intervals are found for $MPS_{RW,max}$, with the maximal width being 14% of the corresponding $LHS_{300}$ min-max interval.

### *D.3. Discussion*

The width of the intervals ranged up to 53%, i.e. for $U_{DM,max}$, relative to the min-max range of $LHS_{300}$, which is remarkable as constant thickness

parameters and a nearly constant $PWV_{ref}$, with a maximal deviation of 0.0017 m/s, are assumed. This reveals a significant uncertainty in the use of $PWV_{ref}$ as material parameter, superimposed on the uncertainty of not knowing the true $PWV_{ref}$.

**Table D1**
The effect of altering the coupling between the GOH parameters and $PWV_{ref}$ in 10 configurations at diastolic (80 mmHg) and systolic (120 mmHg) pressure. The median value of the difference between $U_{DM,max}$, $U_{RW,max}$, $\Delta U_{max}$ and $MPS_{RW,max}$ in the adapted and the original idealized dissected wall framework, is presented, with positive values indicating an increase in displacement or stress magnitude compared to the original idealized dissected wall framework. The width of the min-max range obtained based on the 10 configurations is expressed with respect to the total $LHS_{300}$ min-max width.

| | GOH-$PWV_{ref}$ coupling | |
|---|---|---|
| Output | Median difference | Min-max width (%) |
| **Diastole** | | |
| $U_{DM,max}$ (mm) | 1.85 | 47 |
| $U_{RW,max}$ (mm) | 2.41 | 44 |
| $\Delta U_{max}$ (mm) | 4.61 | 52 |
| $MPS_{RW,max}$ (MPa) | −0.002 | 11 |
| **Systole** | | |
| $U_{DM,max}$ (mm) | 1.85 | 51 |
| $U_{RW,max}$ (mm) | 2.03 | 45 |
| $\Delta U_{max}$ (mm) | 4.97 | 53 |
| $MPS_{RW,max}$ (MPa) | −0.005 | 14 |

## Appendix E. Supplementary data

Supplementary data to this article can be found online at https://doi.org/10.1016/j.jmbbm.2024.106370.

## References


Alimohammadi, M., Sherwood, J.M., Karimpour, M., Agu, O., Balabani, S., Diaz-Zuccarini, V., 2015. Aortic dissection simulation models for clinical support: fluid-structure interaction vs. rigid wall models. Biomed. Eng. Online 14.

Bäumler, K., Vedula, V., Sailer, A.M., Seo, J., Chiu, P., Mistelbauer, G., Chan, F.P., Fischbein, M.P., Marsden, A.L., Fleischmann, D., 2020. Fluid–structure interaction simulations of patient-specific aortic dissection. Biomech. Model. Mechanobiol. 1–22.

Bersi, M.R., Bellini, C., Wu, J., Montaniel, K.R.C., Harrison, D.G., Humphrey, J.D., 2016. Excessive adventitial remodeling leads to early aortic maladaptation in angiotensin-induced hypertension. Hypertension 67, 890–896.

Bols, J., Taelman, L., De Santis, G., Degroote, J., Verhegghe, B., Segers, P., Vierendeels, J., 2016. Unstructured hexahedral mesh generation of complex vascular trees using a multi-block grid-based approach. Comput. Methods Biomech. Biomed. Eng. 19, 663–672.

Borges, L.D., Jaldin, R.G., Dias, R.R., Stolf, N.A.G., Michel, J.B., Gutierrez, P.S., 2008. Collagen is reduced and disrupted in human aneurysms and dissections of ascending aorta. Hum. Pathol. 39, 437–443.

Borgonovo, E., 2007. A new uncertainty importance measure. Reliab. Eng. Syst. Saf. 92, 771–784.

Brunet, J., Pierrat, B., Badel, P., 2021. A parametric study on factors influencing the onset and propagation of aortic dissection using the extended finite element method. IEEE Trans. Biomed. Eng. 68, 2918–2929.

Chong, M.Y., Gu, B., Chan, B.T., Ong, Z.C., Xu, X.Y., Lim, E., 2020. Effect of intimal flap motion on flow in acute type B aortic dissection by using fluid-structure interaction. International Journal for Numerical Methods in Biomedical Engineering 36, 22.

Dal, H., Acan, A.K., Durcan, C., Hossain, M., 2023. An in silico-based investigation on anisotropic hyperelastic constitutive models for soft biological tissues. Arch. Comput. Methods Eng. 32.

DeMartino, R.R., Sen, I., Huang, Y., Bower, T.C., Oderich, G.S., Pochettino, A., Greason, K., Kalra, M., Johnstone, J., Shuja, F., Harmsen, W.S., Macedo, T., Mandrekar, J., Chamberlain, A.M., Weiss, S., Goodney, P.P., Roger, V., 2018. Population-Based Assessment of the Incidence of Aortic Dissection, Intramural Hematoma, and Penetrating Ulcer, and Its Associated Mortality From 1995 to 2015. Circ. Cardiovasc. Qual. Outcome 11.

Deplano, V., Boufi, M., Gariboldi, V., Loundou, A.D., D'Journo, X.B., Cautela, J., Djemli, A., Alimi, Y.S., 2019. Mechanical characterisation of human ascending aorta dissection. J. Biomech. 94, 138–146.

Eikendal, A.L.M., den Ruijter, H.M., Haaring, C., Saam, T., van der Geest, R.J., Westenberg, J.J.M., Bots, M.L., Hoefer, I.E., Leiner, T., 2018. Sex, body mass index, and blood pressure are related to aortic characteristics in healthy, young adults using magnetic resonance vessel wall imaging: the AMBITYON study. Magnetic Resonance Materials in Physics Biology and Medicine 31, 173–182.

Famaey, N., Vastmans, J., Fehervary, H., Maes, L., Vanderveken, E., Rega, F., Mousavi, S. J., Avril, S., 2018. Numerical simulation of arterial remodeling in pulmonary autografts. ZAMM-Zeitschrift fur Angewandte Mathematik und Mechanik 98, 2239–2257.

Fattori, R., Montgomery, D., Lovato, L., Kische, S., Di Eusanio, M., Ince, H., Eagle, K.A., Isselbacher, E.M., Nienaber, C.A., 2013. Survival after endovascular therapy in patients with type B aortic dissection A report from the international registry of acute aortic dissection (IRAD). JACC Cardiovasc. Interv. 6, 876–882.

Ferraro, M., Trachet, B., Aslanidou, L., Fehervary, H., Segers, P., Stergiopulos, N., 2018. Should we ignore what we cannot measure? How non-uniform stretch, non-uniform wall thickness and minor side branches affect computational aortic biomechanics in mice. Ann. Biomed. Eng. 46, 159–170.

Ganten, M.K., Weber, T.F., von Tengg-Kobligk, H., Bockler, D., Stiller, W., Geisbusch, P., Kauffmann, G.W., Delorme, S., Bock, M., Kauczor, H.U., 2009. Motion characterization of aortic wall and intimal flap by ECG-gated CT in patients with chronic B-dissection. Eur. J. Radiol. 72, 146–153.

Gao, S., van 't Klooster, R., Brandts, A., Roes, S.D., Dehnavi, R.A., de Roos, A., Westenberg, J.J.M., van der Geest, R.J., 2017. Quantification of common carotid artery and descending aorta vessel wall thickness from MR vessel wall imaging using a fully automated processing pipeline. J. Magn. Reson. Imag. 45, 215–228.

Gao, Z.C., Qin, Z.X., Qian, D.H., Pan, W.X., Zhou, G.Q., An, Z.X., Hou, C.C., Wang, L.Y., Zhang, L.Y., Gu, T., Jin, J., 2022. Risk factors for incomplete thrombosis in false lumen in sub-acute type B aortic dissection post-TEVAR. Heart Ves. 37, 505–512.

Gasser, T.C., Ogden, R.W., Holzapfel, G., 2006. Hyperelastic modelling of arterial layers with distributed collagen fibre orientations. Journal of the Royal Society Interface 3, 15–35.

Georgakarakos, E., Ioannou, C.V., Kamarianakis, Y., Papaharilaou, Y., Kostas, T., Manousaki, E., Katsamouris, A.N., 2010. The role of geometric parameters in the prediction of abdominal aortic aneurysm wall stress. Eur. J. Vasc. Endovasc. Surg. 39, 42–48.

Gheysen, L., Maes, L., Famaey, N., Segers, P., 2023. Pulse wave velocity: a clinical measure to aid material parameter estimation in computational arterial biomechanics. J. Biomech. 149, 1–17.

Gpy, 2012. GPy: A Gaussian Process Framework in python.

Gultekin, O., Hager, S.P., Dal, H., Holzapfel, G.A., 2019. Computational modeling of progressive damage and rupture in fibrous biological tissues: application to aortic dissection. Biomech. Model. Mechanobiol. 18, 1607–1628.

Helton, J.C., Davis, F.J., 2003. Latin hypercube sampling and the propagation of uncertainty in analyses of complex systems. Reliab. Eng. Syst. Saf. 81, 23–69.

Herman, J., Usher, W., 2017. SALib: an open-source Python library for sensitivity analysis. J. Open Source Softw. 2, 97.

Holzapfel, G.A., Niestrawska, J.A., Ogden, R.W., Reinisch, A.J., Schriefl, A.J., 2015. Modelling non-symmetric collagen fibre dispersion in arterial walls. Journal of the Royal Society Interface 12, 14.

Horny, L., Adamek, T., Kulvajtova, M., 2014. Analysis of axial prestretch in the abdominal aorta with reference to post mortem interval and degree of atherosclerosis. J. Mech. Behav. Biomed. Mater. 33, 93–98.

Humphrey, J.D., 2013. Possible mechanical roles of glycosaminoglycans in thoracic aortic dissection and associations with dysregulated transforming growth factor-beta. J. Vasc. Res. 50, 1–10.
Iliopoulos, D.C., Kritharis, E.P., Giagini, A.T., Papadodima, S.A., Sokolis, D.P., 2009. Ascending thoracic aortic aneurysms are associated with compositional remodeling and vessel stiffening but not weakening in age-matched subjects. J. Thorac. Cardiovasc. Surg. 137, 101–109.
Jadidi, M., Habibnezhad, M., Anttila, E., Maleckis, K., Desyatova, A., MacTaggart, J., Kamenskiy, A., 2020. Mechanical and structural changes in human thoracic aortas with age. Acta Biomater. 103, 172–188.
Keramati, H., Birgersson, E., Ho, J.P., Kim, S., Chua, K.J., Leo, H.L., 2020. The effect of the entry and re-entry size in the aortic dissection: a two-way fluid-structure interaction simulation. Biomech. Model. Mechanobiol. 19, 2643–2656.
Li, A.E., Kamel, I., Rando, F., Anderson, M., Kumbasar, B., Lima, J.A.C., Bluemke, D.A., 2004. Using MRI to assess aortic wall thickness in the multiethnic study of atherosclerosis: distribution by race, sex, and age. Am. J. Roentgenol. 182, 593–597.
Logghe, G., Trachet, B., Segers, P., De Backer, J., Mulorz, J., Dueppers, P., Vermassen, F., Schelzig, H., Van Herzeele, I., Wagenhauser, M.U., 2021. Outflow through aortic side branches drives false lumen patency in type B aortic dissection. Frontiers in Cardiovascular Medicine 8, 11.
Mani, V., Muntner, P., Gidding, S.S., Aguiar, S.H., El Aidi, H., Weinshelbaum, K.B., Taniguchi, H., van der Geest, R., Reiber, J.H.C., Bansilal, S., Farkouh, M., Fuster, V., Postley, J.E., Woodward, M., Fayad, Z.A., 2009. Cardiovascular magnetic resonance parameters of atherosclerotic plaque burden improve discrimination of prior major adverse cardiovascular events. J. Cardiovasc. Magn. Reson. 11.
Manopoulos, C., Karathanasis, L., Kouerinis, I., Angouras, D.C., Lazaris, A., Tsangaris, S., Sokolis, D.P., 2018. Identification of regional/layer differences in failure properties and thickness as important biomechanical factors responsible for the initiation of aortic dissections. J. Biomech. 80, 102–110.
Mastroroberto, P., Onorati, F., Zofrea, S., Renzulli, A., Indolfi, C., 2010. Outcome of open and endovascular repair in acute type B aortic dissection: a retrospective and observational study. J. Cardiothorac. Surg. 5.
McComb, B.L., Munden, R.F., Duan, F.H., Jain, A.A., Tuite, C., Chiles, C., 2016. Normative reference values of thoracic aortic diameter in American college of radiology imaging network (ACRIN 6654) arm of national lung screening trial. Clin. Imag. 40, 936–943.
Mensel, B., Quadrat, A., Schneider, T., Kuhn, J.P., Dorr, M., Volzke, H., Lieb, W., Hegenscheid, K., Lorbeer, R., 2014. MRI-Based determination of reference values of thoracic aortic wall thickness in a general population. Eur. Radiol. 24, 2038–2044.
Nienaber, C.A., Kische, S., Ince, H., Fattori, R., 2011. Thoracic endovascular aneurysm repair for complicated type B aortic dissection. J. Vasc. Surg. 54, 1529–1533.
Nienaber, C.A., Kische, S., Rousseau, H., 2014. Endovascular repair of type B aortic dissection: long-term results of the randomized investigation of stent grafts in aortic dissection trial. Circulation-cardiovascular interventions 59, 554-554.
Niestrawska, J.A., Haspinger, D.C., Holzapfel, G.A., 2018. The influence of fiber dispersion on the mechanical response of aortic tissues in health and disease: a computational study. Comput. Methods Biomech. Biomed. Eng. 21, 99–112.
Niestrawska, J.A., Viertler, C., Regitnig, P., Cohnert, T.U., Sommer, G., Holzapfel, G.A., 2016. Microstructure and mechanics of healthy and aneurysmatic abdominal aortas: experimental analysis and modelling. Journal of the Royal Society Interface 13, 1–14.
Ogden, R.W., 2017. Nonlinear continuum mechanics and modeling the elasticity of soft biological tissues with a focus on artery walls. Biomechanics: Trends in Modeling and Simulation 20, 83–156.
Peirlinck, M., De Beule, M., Segers, P., Rebelo, N., 2018a. A modular inverse elastostatics approach to resolve the pressure-induced stress state for in vivo imaging based cardiovascular modeling. J. Mech. Behav. Biomed. Mater. 85, 124–133.
Peirlinck, M., Debusschere, N., Iannaccone, F., Siersema, P.D., Verhegghe, B., Segers, P., De Beule, M., 2018b. An in silico biomechanical analysis of the stent-esophagus interaction. Biomech. Model. Mechanobiol. 17, 111–131.
Peterss, S., Mansour, A.M., Ross, J.A., Vaitkeviciute, I., Charilaou, P., Dumfarth, J., Fang, H., Ziganshin, B.A., Rizzo, J.A., Adeniran, A.J., Elefteriades, J.A., 2016. Changing pathology of the thoracic aorta from acute to chronic dissection literature review and insights. J. Am. Coll. Cardiol. 68, 1054–1065.
Pirola, S., Guo, B.L., Menichini, C., Saitta, S., Fu, W.G., Dong, Z.H., Xu, X.Y., 2019. 4-D flow MRI-based computational analysis of blood flow in patient-specific aortic dissection. IEEE Trans. Biomed. Eng. 66, 3411–3419.
Powell, J.T., Vine, N., Crossman, M., 1992. On the accumulation of D-aspartate in elastin and other proteins of the aging aorta. Atherosclerosis 97, 201–208.
Rolf-Pissarczyk, M., Li, K.W., Fleischmann, D., Holzapfel, G.A., 2021. A discrete approach for modeling degraded elastic fibers in aortic dissection. Comput. Methods Appl. Mech. Eng. 373, 21.
Rylski, B., Munoz, C., Beyersdorf, F., Siepe, M., Reser, D., Carrel, T., Schoenhoff, F., Schlensak, C., Lescan, M., Eckstein, H.H., Reutersberg, B., Erbel, R., Janosi, R.A., Czerny, M., 2018. How does descending aorta geometry change when it dissects? Eur. J. Cardio. Thorac. Surg. 53, 815–821.
Schriefl, A.J., Zeindlinger, G., Pierce, D.M., Regitnig, P., Holzapfel, G.A., 2012. Determination of the layer-specific distributed collagen fibre orientations in human thoracic and abdominal aortas and common iliac arteries. Journal of the Royal Society Interface 9, 1275–1286.
Shapiro, S.D., Endicott, S.K., Province, M.A., Pierce, J.A., Campbell, E.J., 1991. Marked longevity of human lung parenchymal elastic fibers deduced from prevalence of D-aspartate and nuclear-weapons related radiocarbon. J. Clin. Invest. 87, 1828–1834.
Sherifova, S., Holzapfel, G.A., 2019. Biomechanics of aortic wall failure with a focus on dissection and aneurysm: a review. Acta Biomater. 99, 1–17.
Sokolis, D.P., 2020. Time-course of axial residual strain remodeling and layer-specific thickening during aging along the human aorta. J. Biomech. 112, 110065.
The Reference Values for Arterial Stiffness' collaboration, 2010. Determinants of pulse wave velocity in healthy people and in the presence of cardiovascular risk factors: 'establishing normal and reference values. Eur. Heart J. 31, 2338–2350.
Trimarchi, S., Tolenaar, J.L., Jonker, F.H.W., Murray, B., Tsai, T.T., Eagle, K.A., Rampoldi, V., Verhagen, H.J.M., van Herwaarden, J.A., Moll, F.L., Muhs, B.E., Elefteriades, J.A., 2013. Importance of false lumen thrombosis in type B aortic dissection prognosis. J. Thorac. Cardiovasc. Surg. 145, S208–S212.
Tsai, T.T., Evangelista, A., Nienaber, C.A., Myrmel, T., Meinhardt, G., Cooper, J.V., Smith, D.E., Suzuki, T., Fattori, R., Llovet, A., Froehlich, J., Hutchison, S., Distante, A., Sundt, T., Beckman, J., Januzzi, J.L., Isselbacher, E.M., Eagle, K.A., 2007. Partial thrombosis of the false lumen in patients with acute type B aortic dissection. N. Engl. J. Med. 357, 349–359.
Wang, L., Hill, N.A., Roper, S.M., Luo, X.Y., 2018. Modelling peeling- and pressure-driven propagation of arterial dissection. J. Eng. Math. 109, 227–238.
Wang, L., Roper, S.M., Hill, N.A., Luo, X.Y., 2017a. Propagation of dissection in a residually-stressed artery model. Biomech. Model. Mechanobiol. 16, 139–149.
Wang, L., Zhu, J., Samady, H., Monoly, D., Zheng, J., Guo, X.Y., Maehara, A., Yang, C., Ma, G.S., Mintz, G.S., Tang, D.L., 2017b. Effects of residual stress, axial stretch, and circumferential shrinkage on coronary plaque stress and strain calculations: a modeling study using IVUS-based near-idealized geometries. Journal of Biomechanical Engineering-Transactions of the Asme 139, 11.
Weisbecker, H., Pierce, D.M., Regitnig, P., Holzapfel, G.A., 2012. Layer-specific damage experiments and modeling of human thoracic and abdominal aortas with non-atherosclerotic intimal thickening. J. Mech. Behav. Biomed. Mater. 12, 93–106.
Wu, D., Shen, Y.H., Russell, L., Coselli, J.S., LeMaire, S.A., 2013. Molecular mechanisms of thoracic aortic dissection. J. Surg. Res. 184, 907–924.
Xie, E.M., Yang, F., Liu, Y., Xue, L., Fan, R.X., Xie, N.A.J., Chen, L.F., Liu, J.T., Luo, J.F., 2021. Timing and outcome of endovascular repair for uncomplicated type B aortic dissection. Eur. J. Vasc. Endovasc. Surg. 61, 788–797.
Yamada, H., Sakata, N., Wada, H., Tashiro, T., Tayama, E., 2015. Age-related distensibility and histology of the ascending aorta in elderly patients with acute aortic dissection. J. Biomech. 48, 3267–3273.
Yamauchi, T., Masai, T., Takano, H., Shirakawa, Y., Toda, K., Sawa, Y., Osaka Cardiovasc Surg Res Grp, O.S.C., 2018. Equations for estimating the predissected diameter of the descending aorta from computed tomographic images at the onset of aortic dissection. J. Am. Heart Assoc. 7, 1–14.
Yang, S.F., Li, X., Chao, B.T., Wu, L.B., Cheng, Z.P., Duan, Y.H., Wu, D.W., Zhan, Y.Q., Chen, J.H., Liu, B., Ji, X.P., Nie, P., Wang, X.M., 2014. Abdominal aortic intimal flap motion characterization in acute aortic dissection: assessed with retrospective ECG-gated thoracoabdominal aorta dual-source CT angiography. PLoS One 9, 9.
Zhang, M., Liu, H.F., Cai, Z.X., Sun, C.R., Sun, W., 2022. A novel framework for quantifying the subject-specific three-dimensional residual stress field in the aortic wall. J. Mech. Behav. Biomed. Mater. 125, 11.